OPEN ACCESS



Dissipative Dark Matter on FIRE. II. Observational Signatures and Constraints from Local Dwarf Galaxies

Xuejian Shen 10, Philip F. Hopkins 10, Lina Necib^{2,3}0, Fangzhou Jiang 1,40, Michael Boylan-Kolchin 50, and Andrew Wetzel 1 TAPIR, California Institute of Technology, Pasadena, CA 91125, USA; xshen@caltech.edu

2 Kavli Institute for Astrophysics and Space Research, Massachusetts Institute of Technology, 77 Massachusetts Avenue, Cambridge MA 02139, USA

3 The NSF AI Institute for Artificial Intelligence and Fundamental Interactions, USA

4 Carnegie Observatories, 813 Santa Barbara Street, Pasadena, CA 91101, USA

5 Department of Astronomy, The University of Texas at Austin, 2515 Speedway Stop C1400, Austin, TX 78712, USA

6 Department of Physics & Astronomy, University of California, Davis, CA 95616, USA

Received 2023 June 1; revised 2024 February 29; accepted 2024 March 1; published 2024 April 30

Abstract

We analyze the first cosmological baryonic zoom-in simulations of galaxies in dissipative self-interacting dark matter (dSIDM). The simulations utilize the FIRE-2 galaxy formation physics with the inclusion of dissipative dark matter self-interactions modeled as a constant fractional energy dissipation ($f_{\rm diss}=0.75$). In this paper, we examine the properties of dwarf galaxies with $M_* \sim 10^5 - 10^9 M_\odot$ in both isolation and within Milky Way–mass hosts. For isolated dwarfs, we find more compact galaxy sizes and promotion of disk formation in dSIDM with $(\sigma/m) \leq 1 \, {\rm cm^2 g^{-1}}$. On the contrary, models with $(\sigma/m) = 10 \, {\rm cm^2 g^{-1}}$ produce puffier stellar distributions that are in tension with the observed size–mass relation. In addition, owing to the steeper central density profiles, the subkiloparsec circular velocities of isolated dwarfs when $(\sigma/m) \geq 0.1 \, {\rm cm^2 g^{-1}}$ are enhanced by about a factor of 2, which are still consistent with the kinematic measurements of Local Group dwarfs but in tension with the H I rotation curves of more massive field dwarfs. Meanwhile, for satellites of Milky Way–mass hosts, the median circular velocity profiles are marginally affected by dSIDM physics, but dSIDM may help promote the structural diversity of dwarf satellites. The number of satellites is slightly enhanced in dSIDM, but the differences are small compared with the large host-to-host variations. In conclusion, the dSIDM models with $(\sigma/m) \gtrsim 0.1 \, {\rm cm^2 g^{-1}}$, $f_{\rm diss} = 0.75$ are in tension in massive dwarfs $(M_{\rm halo} \sim 10^{11} M_\odot)$ due to circular velocity constraints. However, models with lower effective cross sections (at this halo mass/velocity scale) are still viable and can produce nontrivial observable signatures.

Unified Astronomy Thesaurus concepts: Hydrodynamical simulations (767); Cosmology (343); Dark matter (353); Dwarf galaxies (416); Local Group (929)

1. Introduction

The nature of dark matter is a fundamental question in modern cosmology. In the standard model of cosmology, the ΛCDM model, dark matter is assumed to be nonrelativistic (cold) at decoupling from the initial plasma and effectively collisionless. It only interacts via gravity and acts as the driver for cosmic structure formation. This picture has been successful in describing the large-scale structures in the Universe (e.g., Blumenthal et al. 1984; Davis et al. 1985) and forms the foundation for theories of galaxy formation and evolution (e.g., White & Frenk 1991; Kauffmann et al. 1993; Cole et al. 2000). In terms of particle nature, the Weakly Interacting Massive Particles (WIMPs) provide a compelling class of cold dark matter (CDM) candidates, well motivated from beyondstandard-model physics (see the review Bertone et al. 2005, and references therein). However, despite decades of efforts in direct/indirect detection or collider searches for WIMPs, there is no confirmed signal, and the WIMP parameter space is becoming increasingly constrained (e.g., Bertone 2010; Aprile et al. 2012; Akerib et al. 2014; Aprile et al. 2018; Aalbers et al. 2023). As a result, a spectrum of alternative dark matter models to WIMP-like CDM has been brought into view (e.g., Hogan &

Original content from this work may be used under the terms of the Creative Commons Attribution 4.0 licence. Any further distribution of this work must maintain attribution to the author(s) and the title of the work, journal citation and DOI.

Dalcanton 2000; Spergel & Steinhardt 2000; Dalcanton & Hogan 2001; Frenk & White 2012; Buckley & Peter 2018).

Meanwhile, astrophysical observations have revealed anomalies at small scales (see the review Bullock & Boylan-Kolchin 2017) primarily in Local dwarf galaxies, which tentatively suggest non-CDM physics. A classic example of this is the missing satellites (MS) problem: the dark matter subhalos of Milky Waymass galaxies in dark-matter-only (DMO) simulations significantly outnumber the observed satellites around the real Milky Way (e.g., Klypin et al. 1999; Moore et al. 1999). In addition, there is a mismatch between the inner structures of subhalos in simulations and the observed satellites. The too-big-to-fail (TBTF) problem states that a substantial population of massive, concentrated subhalos produced in DMO simulations is missing in the observed satellites or field dwarfs in the Local Group (Boylan-Kolchin et al. 2011, 2012; Garrison-Kimmel et al. 2014; Kirby et al. 2014; Tollerud et al. 2014) and beyond (Papastergis et al. 2015). A qualitatively similar problem for field dwarfs is the core-cusp (CC) problem: the central density profiles of lowsurface-brightness galaxies (LSBs) are cored (e.g., Flores & Primack 1994; Moore 1994; de Blok et al. 2001; Gentile et al. 2004; Simon et al. 2005; Kuzio de Naray et al. 2006; Spano et al. 2008; Kuzio de Naray & Kaufmann 2011; Kuzio de Naray & Spekkens 2011; Oh et al. 2011; Walker & Peñarrubia 2011; Chan et al. 2015; Oh et al. 2015; Lelli et al. 2016b; Zhu et al. 2016; Genzel et al. 2020; Li et al. 2020). This is contradictory to the universal cuspy central profile found in DMO simulations

(Navarro et al. 1996, 1997; Moore et al. 1999; Klypin et al. 2001; Navarro et al. 2004; Diemand et al. 2005).

In recent years, the TBTF and CC problems have evolved to the diversity problem, which was first proposed for field dwarfs (Oman et al. 2015), later extended to Milky Way satellites (Kaplinghat et al. 2019). The diversity of the dwarf galaxy structures is not well reproduced (e.g., Santos-Santos et al. 2018, 2020; Garrison-Kimmel et al. 2019a; Jiang et al. 2019; Sales et al. 2022) by simply adjusting the strength/numeric scheme of baryonic feedback or variations of environmental effects in the CDM framework.

Self-interacting dark matter (SIDM), as an important category of alternative dark matter models, has been proposed and discussed in the literature for about three decades (e.g., Carlson et al. 1992; de Laix et al. 1995; Firmani et al. 2000; Spergel & Steinhardt 2000). SIDM is well motivated by hidden dark sectors as extensions to the standard model (e.g., Ackerman et al. 2009; Arkani-Hamed et al. 2009; Feng et al. 2009, 2010; Loeb & Weiner 2011; van den Aarssen et al. 2012; Cyr-Racine & Sigurdson 2013; Tulin et al. 2013; Cline et al. 2014; Hryczuk & Jodłowski 2020; Cyr-Racine et al. 2022). Self-interactions of dark matter particles could thermalize the inner halo region, resulting in an isothermal central core, which could potentially address some small-scale problems (see the review of Tulin & Yu 2018, and references therein).

Early DMO SIDM simulations have found that a selfinteraction cross section of $\sim 1~\text{cm}^2~\text{g}^{-1}$ could address the CC and TBTF problems in dwarf galaxies (e.g., Vogelsberger et al. 2012; Rocha et al. 2013; Zavala et al. 2013; Elbert et al. 2015). In recent years, SIDM models with comparable cross sections were shown to enhance (e.g., Creasey et al. 2017; Kamada et al. 2017; Kahlhoefer et al. 2019; Sameie et al. 2020) the diversity of rotation curves of field dwarfs (Oman et al. 2015; Kaplinghat et al. 2020) and the diverse central densities of Local Group satellites (Kaplinghat et al. 2019). Since the constant density cores of dwarf satellites in SIDM make them more susceptible to tidal disruption (e.g., Peñarrubia et al. 2010; Dooley et al. 2016) and "evaporation" through interactions with host halo particles (e.g., Vogelsberger et al. 2019), the abundance and spatial distribution of satellites could also be affected, which connects to the MS problem.

The astrophysical studies of SIDM mentioned above rely on elastic dark matter self-interactions. However, generic particle physics realizations of SIDM could host inelastic (or specifically dissipative) self-interactions (e.g., Arkani-Hamed et al. 2009; Alves et al. 2010; Kaplan et al. 2010; Loeb & Weiner 2011; Cyr-Racine & Sigurdson 2013; Boddy et al. 2014; Cline et al. 2014; Wise & Zhang 2014; Foot & Vagnozzi 2015a; Schutz & Slatyer 2015; Boddy et al. 2016; Finkbeiner & Weiner 2016; Blennow et al. 2017; Zhang 2017; Das & Dasgupta 2018; Gresham et al. 2018; Cyr-Racine et al. 2022). Dissipative self-interactions are often associated with a more complex "dark sector" with multiple components, such as hidden valleys (Strassler & Zurek 2007), the twin Higgs model (e.g., Chacko et al. 2006, 2017), composite bound by strong forces (Boddy et al. 2014), and atomic dark matter (Mohapatra & Teplitz 2000; Foot 2004; Kaplan et al. 2010). Despite the theoretical motivations, the impact of dissipative processes of dark matter is rarely explored in the context of cosmological structure formation.

Indeed, in previous studies, the focus on purely elastic SIDM (eSIDM) was largely driven by its application in explaining the

small-scale problems through kinematically heating dark matter and lowering central halo densities. However, other processes can strongly influence these properties. For instance, gas outflows driven by stellar/supernovae feedback could help generate dark matter cores (Governato et al. 2010, 2012; Pontzen & Governato 2012; Madau et al. 2014), a process that has been verified in CDM simulations with baryons (e.g., Brooks & Zolotov 2014; Dutton et al. 2016; Fattahi et al. 2016; Sawala et al. 2016; Wetzel et al. 2016; Garrison-Kimmel et al. 2019a; Buck et al. 2019; Lazar et al. 2020; Sales et al. 2022). In subsequent eSIDM simulations with baryons (e.g., Vogelsberger et al. 2014; Elbert et al. 2015; Fry et al. 2015; Robles et al. 2017; Despali et al. 2019; Fitts et al. 2019; Robles et al. 2019), the distinct signatures of eSIDM were found to be substantially reduced with the inclusion of baryons, and, in certain regimes, a baryon-driven core formation can dominate over dark matter physics. In principle, baryonic effects could mitigate or even completely hide exotic dark matter physics that would otherwise lead to enhanced central densities in DMO simulations. Therefore, as an example of such models, the parameter space for dSIDM is more widely open than previously believed. Beyond that, the halo contraction driven by dissipative interactions produces compact dwarfs and/or promotes the diversity of dwarf galaxy rotation curves to the observed level.

Meanwhile, continuous improvements in observations of local dwarf galaxies and other small-scale baryonic structures have enabled great opportunities to constrain the nature of dark matter. For example, the census of ultrafaint satellite galaxies in the Local Group through optical imaging surveys has been boosted in recent years, using the data from the Dark Energy Survey (DES; Bechtol et al. 2015; Drlica-Wagner et al. 2015; Dark Energy Survey Collaboration et al. 2016; Drlica-Wagner et al. 2020; Nadler et al. 2020b), the Panoramic Survey Telescope and Rapid Response System (Pan-STARRS; Laevens et al. 2015a, 2015b), and others (e.g., Torrealba et al. 2016, 2019). Many of the recently detected ultrafaints appear to be clustered around the Large Magellanic Cloud (LMC; Drlica-Wagner et al. 2015; Koposov et al. 2015). These candidate LMC satellites are attractive targets for ongoing and future observations to test the Λ CDM model (Wheeler et al. 2015). The stellar mass and luminosity functions of these Local Group satellites have been used to update constraints of a variety of alternative dark matter models (e.g., Nadler et al. 2019; Enzi et al. 2021; Nadler et al. 2021). Meanwhile, the structural and dynamical properties of the Local Group satellites with resolved stellar populations have been measured (see for example compilations by McConnachie 2012; Tollerud et al. 2014; Lovell & Zavala 2023, and references therein) and play a key role in understanding the TBTF problem (Boylan-Kolchin et al. 2011).

In the near future, the Legacy Survey of Space and Time (LSST; LSST Science Collaboration et al. 2009) at the Vera Rubin Observatory has the potential to substantially expand the discovery space of faint dwarf galaxies, being sensitive to galaxies 100 times fainter than Sloan Digital Sky Survey (SDSS; York et al. 2000) at the same distance (Bullock & Boylan-Kolchin 2017). Beyond the Local Group, the Dark Energy Camera (Flaugher et al. 2015) and Subaru (Hyper) Suprime-Cam (e.g., Miyazaki et al. 2002, 2018) are being used to search for faint companions of nearby galaxies (e.g., Sand et al. 2015; Carlin et al. 2016; Crnojević et al. 2016), as well as

the LSBs and ultradiffuse dwarf galaxies (UDGs) in cluster environments (e.g., Koda et al. 2015; Mihos et al. 2015; Muñoz et al. 2015; van Dokkum et al. 2015; Eigenthaler et al. 2018). In addition, for relatively massive disky dwarfs (late-type), radio observations have reported the H I rotation curves and mass models of a few hundred of them in the Local Universe (e.g., Oh et al. 2011; Ott et al. 2012; Oh et al. 2015; Lelli et al. 2016b). The time is therefore ripe to make testable predictions from different dark matter model parameter spaces.

In Shen et al. (2021, hereafter Paper I) of this series, we have introduced the first suite of cosmological hydrodynamical zoom-in simulations of galaxies in dSIDM. The simulations employ the Feedback In Realistic Environments (FIRE)-2 model (Hopkins et al. 2018) for hydrodynamics and galaxy formation physics, and the dSIDM model is empirically parameterized by a dimensionless dissipation factor and a constant (or velocity-dependent) self-interaction cross section. We explored the parameter choices that lead to weakly collisional $((\sigma/m) \lesssim 10 \, \text{cm}^2 \, \text{g}^{-1})$ and weakly dissipative (cooling time much longer than that of dense baryonic gas counterpart) dark fluids on cosmological scales. Similar "effective" dSIDM models have been explored using semianalytical methods and idealized simulations (Essig et al. 2019; Huo et al. 2020). We stress that this type of model is qualitatively different from the dissipative dark matter proposed by many other studies (Fan et al. 2013; Foot 2013; Randall & Scholtz 2015; Roy et al. 2023), which are highly coupled (effective "collision" rate, $\Gamma_{\rm eff} \gg H$, H is the Hubble parameter) and highly dissipative (similar to the cooling in the baryonic sector) and will likely give rise to disk-like structures or fragmentation to "compact" objects (Gemmell et al. 2023). In Paper I, we have identified several distinct properties of dwarf galaxies in dSIDM, including the steepening of the central density profile, enhanced rotation support of dark matter, and the deformation of halos to become oblate in shape. These unique structural and kinematic properties are expected to give observational signatures that could be used to constrain dSIDM models.

In this paper, we make predictions for various observed properties of galaxies in dSIDM and compare them to the observed dwarf satellite galaxies in the Local Group or LSBs in the field. The paper will be organized as follows: In Section 2, we briefly review the simulation setup and the dark matter models studied. In Section 3, we present predictions for the stellar content of the simulated dwarfs, including density profiles, size, and mock optical images. Then, in Section 4, the circular velocity profiles of the simulated dwarfs (or satellites of Milky Way–mass hosts) will be compared with their observational counterparts specifically. In Section 5, the satellite counts of simulated Milky Way–mass hosts will be studied. Finally, in Section 6, the summary and conclusions will be presented.

2. Methods

2.1. Overview of the Simulation Suite

The analysis in this paper is based on the FIRE-2 dSIDM simulation suite introduced in Paper I, which consists of ~ 40 cosmological hydrodynamical zoom-in simulations of galaxies chosen at representative mass scales with CDM, eSIDM, and dSIDM models. Below, we will give a brief introduction to the simulations and refer the readers to Paper I for more details.

Table 1Simulations of the FIRE-2 dSIDM Suite

Simulation Name	$M_{ m halo}^{ m cdm} \ (M_{\odot})$	R _{vir} cdm (kpc)	$M_*^{ m cdm} \ (M_\odot)$	$r_{1/2}^{ m cdm} \ m (kpc)$	r _{dm} conv (pc)
Ultrafaint dwarf					
m09	2.5e9	35.6	7.0e4	0.46	65
Classical dwarfs					
m10b	9.4e9	55.2	5.8e5	0.36	77
m10q	7.5e9	51.1	1.7e6	0.72	73
m10v	8.5e9	53.5	1.4e5	0.32	65
Bright dwarfs					
m11a	3.6e10	86.7	3.7e7	1.2	310
m11b	4.2e10	90.7	4.2e7	1.7	250
$m11q^a$	1.5e11	138.7	2.9e8	3.1	240
Milky Way-mass h	osts				
m11f	4.5e11	200.2	1.0e10	2.9	280
m12i l.r.	1.1e12	272.3	1.1e11	2.0	290
m12f l.r.	1.5e12	302.8	1.3e11	4.1	310
m12m l.r.	1.5e12	299.3	1.4e11	6.1	360
m12i h.r.	9.8e11	259.9	2.4e10	3.7	150

Note. The simulated galaxies are labeled and grouped by their halo masses. They are classified into four categories: ultrafaint dwarfs; classical dwarfs, with typical halo mass $\leq 10^{10} M_{\odot}$; bright dwarfs, with typical halo mass $\sim 10^{10-11} M_{\odot}$; Milky Way-mass galaxies, with typical halo mass $\sim 10^{12} M_{\odot}$. These halos are randomly picked from the standard FIRE-2 simulation suite (Hopkins et al. 2018), sampling various star formation and merger histories. All units are physical. (1) Name of the simulation. "l.r." ("h.r.") indicates a low (high)-resolution version of the simulation. Typically, the high-resolution version has 8 times better mass resolution. (2) $M_{\rm halo}^{\rm cdm}$, $R_{\rm vir}^{\rm cdm}$: virial mass and virial radius of the halo (defined using the overdensity criterion introduced in Bryan & Norman 1998) in the CDM simulation with baryons at z = 0. (3) M_*^{cdm} , $r_{1/2}^{\text{cdm}}$: galaxy stellar mass and galaxy stellar half mass-radius (defined using stellar particles within 0.1 $R_{\rm vir}$) in the CDM simulation at z = 0. (4) $r_{\rm dm}^{\rm conv}$: Radius of convergence in dark matter properties at z = 0 (calculated for the CDM DMO simulations in the standard FIRE-2 series based on the Power et al. 2003 criterion). As shown in Hopkins et al. (2018), the convergence radii in simulations with baryons can in fact extend to much smaller radii.

The simulations are part of the FIRE (Hopkins et al. 2014) project, specifically the "FIRE-2" version described in Hopkins et al. (2018). The simulations adopt the code GIZMO (Hopkins 2015), with gravity solved using the Tree-PM method (Springel 2005) and hydrodynamics solved using the mesh-free Lagrangian Godunov meshless finite mass (MFM) method. The FIRE galaxy formation physics and numerical parameters are identical to those described in Hopkins et al. (2018), Garrison-Kimmel et al. (2019b). A full list of the galaxies simulated and relevant parameters are shown in Table 1. They are classified by their halo masses to ultrafaint dwarfs, classical dwarfs, bright dwarfs, and Milky Way-mass galaxies. We note that the term "bright dwarf" is inherited from other FIRE studies (Lazar et al. 2020), which are analogs of field LSB galaxies.

As an advanced galaxy formation model, FIRE-2 notably encompasses (1) heating and cooling of gas down to low

^a The galaxy m11q does not have the $(\sigma/m) = 10 \text{ cm}^2 \text{ g}^{-1}$ simulation since it stalls at fairly high redshift due to the formation of dense dark matter clumps at the center of the halo (see Table 1 in Paper I).

We note that the CDM runs are rerun to exactly match the configuration of dSIDM runs (e.g., code version, computing facility, compilers, libraries, and number of MPI tasks), so galaxy properties are not expected to be "identical" to the original FIRE-2 results.

temperatures (10 K) under a redshift-dependent ionizing photon background (Faucher-Giguère et al. 2009), (2) an explicit star formation recipe in dense, self-gravitating, Jeans-unstable, molecular-phase gas (Hopkins et al. 2013), and (3) multiple channels of feedback including stellar winds, supernovae, and radiative feedback (Hopkins et al. 2014). All stellar evolution and feedback inputs are taken directly from stellar evolution models (Leitherer et al. 1999), without subsequent "parameter tuning." Paired with the high mass and spatial resolution of the simulations, the multiphase structure of the interstellar medium (ISM) is resolved. In a series of papers, it has been shown that cosmological zoom-in simulations incorporating these physics can reproduce a diverse range of galaxy properties at a wide range of redshifts, including, e.g., galaxy stellar mass and main sequence (Hopkins et al. 2014, 2018; Feldmann et al. 2023), feedbackdriven galactic outflows (e.g., Muratov 2015; Anglés-Alcázar et al. 2017a), properties of the circumgalactic medium (e.g., Hafen et al. 2019; Stern et al. 2021), mass-metallicity relation (Ma et al. 2016), structural and kinematic properties of dwarf galaxies (e.g., Chan et al. 2015; Oñorbe et al. 2015), and Local Group satellites (e.g., Garrison-Kimmel et al. 2019a; Samuel et al. 2020).

These add the confidence of using FIRE as a basis for studying observational signatures of alternative dark matter models. Nevertheless, we need to warn about the limitations of the FIRE-2 model as a single representation of star formation and feedback models. Stellar feedback-driven gas outflows can drive the formation of cores in dwarf galaxies (e.g., Di Cintio et al. 2014; Chan et al. 2015; Lazar et al. 2020). Despite the census on the most favorable dwarf galaxy mass range for core formation, the exact minimum mass scale where cores show up and the diversity of dwarf galaxy structures depend on the implementation of stellar and supernovae feedback models, which are still open questions. We refer readers to Lazar et al. (2020), Sales et al. (2022), and Despali et al. (2019; specifically on interplay with SIDM models) for a more thorough discussion on this. However, as found in Paper I, the structure of dark matter halos in dSIDM models is much less sensitive to baryonic feedback compared to their CDM counterparts. Testing the coupling of dark matter physics and baryonic physics in a more flexible context and varying the feedback treatment are beyond the scope of the current paper. In addition, there are known missing physics ingredients, especially cosmic rays and feedback from active galactic nuclei in the FIRE-2 model (discussed thoroughly in the recent FIRE-3 update, Hopkins et al. 2023b). However, we note these physics are likely not important for the galaxy properties at dwarf to Milky Way mass scale (e.g., Anglés-Alcázar et al. 2017b; Hopkins et al. 2020, 2021; Wellons et al. 2023).

2.2. Dark Matter Model

Dark matter self-interactions are simulated in a Monte-Carlo fashion following the implementation in Rocha et al. (2013; see Appdenix B for details of the SIDM implementation). A simplified, empirical dissipation model is employed: two interacting dark matter particles lose a constant fraction (the dissipation factor $f_{\rm diss}$) of their kinetic energy in the center-of-momentum frame when they collide with each other. The extreme version of this type of interaction is the fusion process (i.e., $f_{\rm diss} = 1$) of dark matter composites discussed in the context of self-interacting asymmetric dark matter (e.g., Detmold et al. 2014; Wise & Zhang 2014; Krnjaic & Sigurdson 2015; Wise & Zhang 2015; Gresham et al. 2018)

and specifically the dark "nuggets" model (Wise & Zhang 2014; Gresham et al. 2018). It is worth noting that there are other particle physics models for dSIDM (e.g., Alves et al. 2010; Kaplan et al. 2010; Fan et al. 2013; Boddy et al. 2014; Cline et al. 2014; Foot & Vagnozzi 2015b; Schutz & Slatyer 2015) with potentially different behaviors on cosmological scales that are not captured by this simplified parameterization. However, it is a reasonable starting point to study the phenomenology of dissipative dark matter in cosmic structure formation.

The simulations employed a fiducial dissipation factor $f_{\rm diss} = 0.75$, and we explore models with constant self-interaction cross section $(\sigma/m) = 0.1$, 1, 10 cm² g⁻¹, or a velocity-dependent cross-sectional model

$$\frac{\sigma(v)}{m} = \frac{(\sigma/m)_0}{1 + (v/v_0)^4},\tag{1}$$

where the fiducial choice is $(\sigma/m)_0 = 10 \text{ cm}^2 \text{ g}^{-1}$, and $v_0 = 10 \,\mathrm{km \, s^{-1}}$. The velocity dependence of the self-interaction cross section is empirically motivated by the relatively tight constraints on SIDM at galaxy cluster scale (e.g., Markevitch et al. 2004; Randall et al. 2008; Kaplinghat et al. 2016) and the relatively high cross section needed to strongly influence some small-scale galaxy properties (e.g., Vogelsberger et al. 2012; Rocha et al. 2013; Zavala et al. 2013; Elbert et al. 2015; Kaplinghat et al. 2016). The velocity dependence is also a generic feature of many particle physics models for SIDM (e.g., Feng et al. 2009; Kaplan et al. 2010; Cyr-Racine & Sigurdson 2013; Boddy et al. 2014; Cline et al. 2014; Boddy et al. 2016; Zhang 2017; Tulin & Yu 2018). In this work, we assume scatterings to be isotropic. Angular dependence can arise when the force mediator is light or massless (e.g., Feng et al. 2009; Cyr-Racine & Sigurdson 2013; Boddy et al. 2016) but the effects are limited for isolated halos (e.g., Robertson et al. 2017).

Given the choices of cross section and dissipation factor, the typical collision and energy dissipation (*cooling*) timescale of dark matter will be smaller than the Hubble timescale but still larger than the dynamical timescale (see Paper I for details). This is different from the baryonic gas in the ISM, for which the cooling time could drop below the dynamical time and experience fragmentation. We do not expect the fragmentation and formation of *compact* dark objects in the dSIDM models studied here. In this paper, we will refer to the dSIDM model with constant cross section $(\sigma/m) = 0.1$, 1, $10 \text{ cm}^2 \text{ g}^{-1}$ as dSIDM-c0.1, 1, 10 for simplicity. For comparison, a subset of the galaxies in the suite is also simulated with the eSIDM model with the constant cross section $(\sigma/m) = 1 \text{ cm}^2 \text{ g}^{-1}$.

2.3. Host Halo and Substructures

The simulations in this suite are all identified with the main *target* halo around which the high-resolution (h.r.) zoom-in region is centered. The central position and velocity of this main halo are defined by the center of mass (of dark matter

 $[\]overline{8}$ The value presented in Paper I was misquoted as 0.5, which is the momentum reduction factor. However, none of the results in Paper I are affected. Since $f_{\rm diss}$ was used as a constant across all simulations, it does not influence the comparisons between simulations. The difference in $f_{\rm diss}$ also does not affect our qualitative conclusions based on the relevant timescales.

The self-interaction cross section is the total cross section, $\int (d\sigma/d\Omega)d\Omega$, throughout this paper.

particles) and are calculated via an iterative zoom-in approach (as described in Wetzel et al. 2023), also known as the shrinking sphere approach (e.g., Power et al. 2003). However, specifically for the measurements of stellar density profiles and galaxy visible sizes, we use stellar particles for the center identification. The bulk properties of the halo and the galaxy it hosts are calculated following the practice of the standard FIRE-2 simulations, as described in Hopkins et al. (2018). We define the halo mass $M_{\rm halo}$ and the halo virial radius $R_{\rm vir}$ using the redshift-dependent overdensity criterion in Bryan & Norman (1998). We define the stellar mass M_* as the total mass of all the stellar particles within an aperture of $0.1\,R_{\rm vir}$ at z=0 and correspondingly define the stellar-half-mass-radius $r_{1/2}$ as the radius that encloses half of the total stellar mass.

To identify substructures in postprocessing, we take two steps following Wetzel et al. (2016), Garrison-Kimmel et al. (2019a), Necib et al. (2019), and Samuel et al. (2020). We first identify bound dark matter subhalos (of the main "target" halo) using the ROCKSTAR (Behroozi et al. 2013) halo finder, ¹⁰ based only on dark matter particles. The force resolution of ROCKSTAR is conservatively set to be the same as the softening length of dark matter particles in simulations.

In the second step, the stellar particles are assigned to the identified dark subhalos through an iterative method (Wetzel et al. 2016; Garrison-Kimmel et al. 2019a; Samuel et al. 2020; Wetzel & Garrison-Kimmel 2020). Initially, the stellar particles are assigned to a dark matter subhalo with a generous cut on their distances to the subhalo center ($r \le 0.8 \, R_{200,\mathrm{m}}$ and $r \le 30 \, \mathrm{kpc}$). Subsequently, stellar particles are iteratively removed if $r < 1.5 \, r_{90}$, where r_{90} is the radius that encloses 90% of the stellar mass currently associated with the subhalo, or if $v < 2\sigma_{v,*}^{3d}$, where $\sigma_{v,*}^{3d}$ is the 3D velocity dispersion of stars currently associated with the number of stellar particles selected stabilizes at the 1% level.

We define M_* of the subhalo as the mass sum of all the stellar particles that remain assigned to each galaxy in this way and correspondingly define $r_{1/2}$ as the radius within which the enclosed mass is $M_*/2$. In all our analysis of subhalos in this paper, we only consider identified subhalos as *satellites* if their distance from the center of the simulated Milky Way/M31-analogue is $20 \,\mathrm{kpc} \leqslant d \leqslant 300 \,\mathrm{kpc}$. Meanwhile, to exclude misidentified subhalos with a limited number of particles, we only keep satellites with a minimum dark matter particle number $N_{\mathrm{dm}} \geqslant 200$ and an associated stellar particle number $N_* \geqslant 10$, which roughly corresponds to a stellar-mass cut of $M_* \geqslant 7 \times 10^4 \, (5.6 \times 10^5) M_{\odot}$ for high-(low-)resolution simulations. For reference, the minimum stellar mass of the observed sample we select (as discussed in Section 4.1) is $7.3 \times 10^4 M_{\odot} \, (3 \times 10^5 M_{\odot})$ for M31 (Milky Way).

2.4. Density Profiles and Rotation Curves

For the main target halos, the spherically averaged density profile $\rho(r)$ is constructed in 40 logarithmically spaced bins from $0.03\,r_{1/2}$ to $R_{\rm vir}$. For satellites of simulated Milky Way–

mass galaxies, this is adjusted to 40 logarithmically spaced bins from 0.1 to 20 kpc. We expected the systematic uncertainties in the binned density estimates to be minimal due to the large number of particles in each simulation sample. The same radial bins are used to measure the rotation curves of simulated galaxies, defined as $V_{\rm circ} \equiv \sqrt{G \, M_{\rm tot}(< r)/r}$, where $M_{\rm tot}(< r)$ is the total mass of the halo within radius r.

3. Galaxy Baryonic Content

3.1. Galaxy Morphology

In Figures 1 and 2, we show images of simulated dwarf galaxies at z = 0, grouped as classical and bright dwarfs. Each image is a red, green, blue (RGB) composite, with the blue, green, red channels corresponding to the SDSS u, g, r bands. The pixel brightness in each channel scales logarithmically with the surface brightness in corresponding bands. The images are generated using the publicly available visualization code¹ (as described in Section 3.1 of Hopkins et al. 2012). To be specific, we use the STARBURST99 model (Leitherer et al. 1999) to determine the spectral energy distribution (SED) of each stellar particle based on its age and initial metallicity. Therefore, the younger stellar population will appear bluer in the images. For each stellar particle, we evaluate the gas column density for the chosen viewing angle, convert that to the dust column density assuming a dust-to-metal ratio of 0.4, and adopt a Milky Way-like reddening curve (as tabulated in Pei 1992). We note that the impact of dust is in fact negligible in these dwarf galaxies. The face-on projections are determined based on the total angular momentum of stellar particles (for Figure 1) or gas particles (for Figure 2) within the field of view. We do not model the point-spread function of observational instruments here.

For the classical dwarfs (m10 galaxies) in Figure 1, the dSIDM-c1 and the velocity-dependent model produce visibly more concentrated stellar content than the CDM case. The contraction of the stellar content is likely related to the contraction of the underlying dark matter distribution. In Paper I, we found cuspier central density profiles of dwarf galaxies in dSIDM models when $(\sigma/m) \gtrsim 0.1 \text{ cm}^2 \text{ g}^{-1}$. This steepening happens typically at $r \lesssim 0.5$ kpc (1 kpc) in classical (bright) dwarfs, which are comparable to the size of the stellar distribution. On the other hand, the dSIDM-c10 model produces fluffier stellar content in m10q. This phenomenon is likely related to the lowered normalization of the central dark matter density profile, and thus shallower gravitational potential, in this model as found and described in Paper I. However, in the same model, the stellar content of m10v is still compact, which demonstrates the large galaxy-to-galaxy variations of the star formation and corresponding dark matter and galaxy dynamics in classical dwarfs. This variation mainly comes from the distinct star formation histories (SFHs) of the two dwarfs. As will be shown in the following section (see also Hopkins et al. 2018), m10q is an early forming galaxy with half of its stellar mass formed at $z \gtrsim 4$ while m10v is late forming with most of its stellar mass formed at $z \lesssim 0.4$, dominated by a few starburst events within the recent 4 Gyr. Therefore, the early formed stars in m10q would have enough time to relax and respond to the change of the underlying dark matter structure, while m10v is still strongly affected by its very recent

¹⁰ The adapted version (Wetzel & Garrison-Kimmel 2020) for GIZMO is at https://bitbucket.org/awetzel/rockstar-galaxies/.

 $^{^{11}}$ $M_{200,m}$ and $R_{200,m}$ are defined for the subhalo with the density criterion 200 times the mean matter density of the Universe at z=0 calculated by ROCKSTAR. Note that this is different from the virial mass definition of the main *target* halo, and is used here only for particle selection purposes.

¹² https://bitbucket.org/phopkins/pfh_python/src/master/

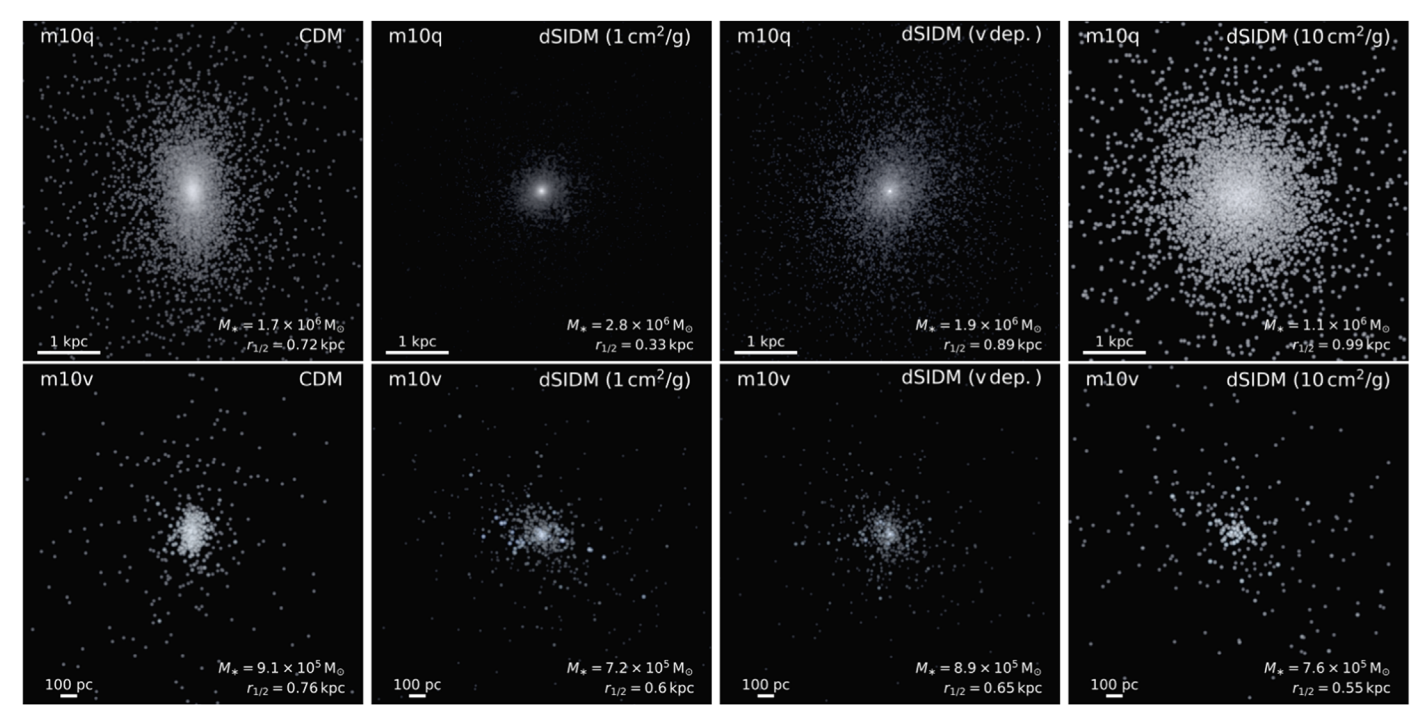


Figure 1. Visualizations of two simulated classical dwarfs. Each column corresponds to one dark matter model studied. The images are mock RGB composites of u, g, r bands with a logarithmic surface-brightness stretch. We use the STARBURST99 model to determine the SED of each stellar particle based on its age and initial metallicity and use ray-tracing (Hopkins et al. 2005) to model dust attenuation assuming a Milky Way-like reddening curve and a dust-to-metal ratio of 0.4. The side lengths of the images are chosen to be $8 \times r_{1/2}$ of the CDM run. The dSIDM models with $(\sigma/m) = 1$ cm² g⁻¹, and the velocity-dependent cross section produces visibly more concentrated stellar content compared to the CDM case (the effective cross section as defined in Paper I of our velocity-dependent model in classical dwarfs is about 0.3 cm² g⁻¹). This is consistent with the more concentrated dark matter distributions in these models found in Paper I. The radius where qualitative changes in the slope of the density profile show up is ~ 0.5 kpc in classical dwarfs, comparable to the size of the stellar distribution. However, the model with $(\sigma/m) = 10$ cm² g⁻¹ produces overall fluffier stellar distribution. This is likely related to the overall decreased density profile normalization in this model due to the development of coherent rotation support.

star formation and feedback. Similar phenomena are found in the stellar density profiles of the two classical dwarfs presented in Figure 4, which will be discussed in Section 3.2.

For the bright dwarfs (m11 galaxies) in Figure 2, we show both face-on and edge-on images because stellar disks start to show up in some simulated galaxies. The viewing angles are determined by the total angular momentum of the stellar particles within half of the field of view. Compared to its CDM counterpart, the dSIDM-c1 model gives rise to thinner and more well-defined stellar disks and meanwhile more concentrated central cusps. This again is in line with the more concentrated underlying dark matter distribution. In Paper I, we found dwarfs in dSIDM models develop cuspy, power-law-like density profiles at galaxy centers that are even steeper than the Navarro-Frenk-White (NFW) profile (compact cusps), which turns out to be insensitive to the self-interaction cross sections or baryonic effects. The morphological transition we observe in the stellar distribution is caused by the stronger central attraction forces provided by the compact cusps formed in dSIDM halos. The central dSIDM cusp provides a well-defined center of the galaxy for star-forming gas to coherently rotate around and also stabilize the thin stellar disk formed. For the velocity-dependent model, the compactness of the stellar content is close to the CDM case because the effective cross section (at the mass scale of bright dwarfs) decreases to \sim 0.01 cm² g⁻¹, which is much smaller than that in the classical dwarfs. Nevertheless, the stellar distribution in this model is more extended, and the ongoing star formation is also suppressed (see the lack of blue star-forming clouds in the

images). For the dSIDM-c10 model, stellar disks are produced but accompanied by apparently fluffier stellar distributions, which is similar to what we described in classical dwarfs.

An important feature of the bright dwarfs is the formation of corotating baryonic structures, e.g., the stellar disks in some of the m11 galaxies, which is absent in lower-mass dwarfs. The larger halo mass and the presence of dense central baryonic components make these galaxies more stable against the energy/momentum injection from feedback, and therefore more able to sustain a rotationally supported gaseous disk (e.g., Obreja et al. 2016; El-Badry et al. 2018). In observations, a highly rotating subset of disky dwarf galaxies (late-type) have been found in H I surveys at a similar mass scale (e.g., Oh et al. 2011, 2015; Lelli et al. 2016b).

In Figure 3, we show the gas surface density projections of the simulated dwarfs in the face-on and edge-on direction (determined by the angular momentum of the gas). The images are composites of the gas surface density in three phases, with the magenta/green/red color representing the *cold* neutral gas with $T \lesssim 8000$ K, the *warm* gas with $T \sim 1-3 \times 10^4$ K and the *hot* ionized gas with $T \gtrsim 10^5$ K, respectively. The cold neutral gas in these dwarf galaxies is confined by the hot circumgalactic medium (CGM) gas, and star formation takes place in dense molecular clouds embedded in the gas disks, and perturbations from subsequent stellar/supernovae feedback manifest as *super bubbles* in the ISM. The feedback heats up the gas at the shock front of *super bubbles* and creates a warm layer in the gas disk. Among all three m11 galaxies simulated in CDM, only m11b develops a well-defined rotating disk

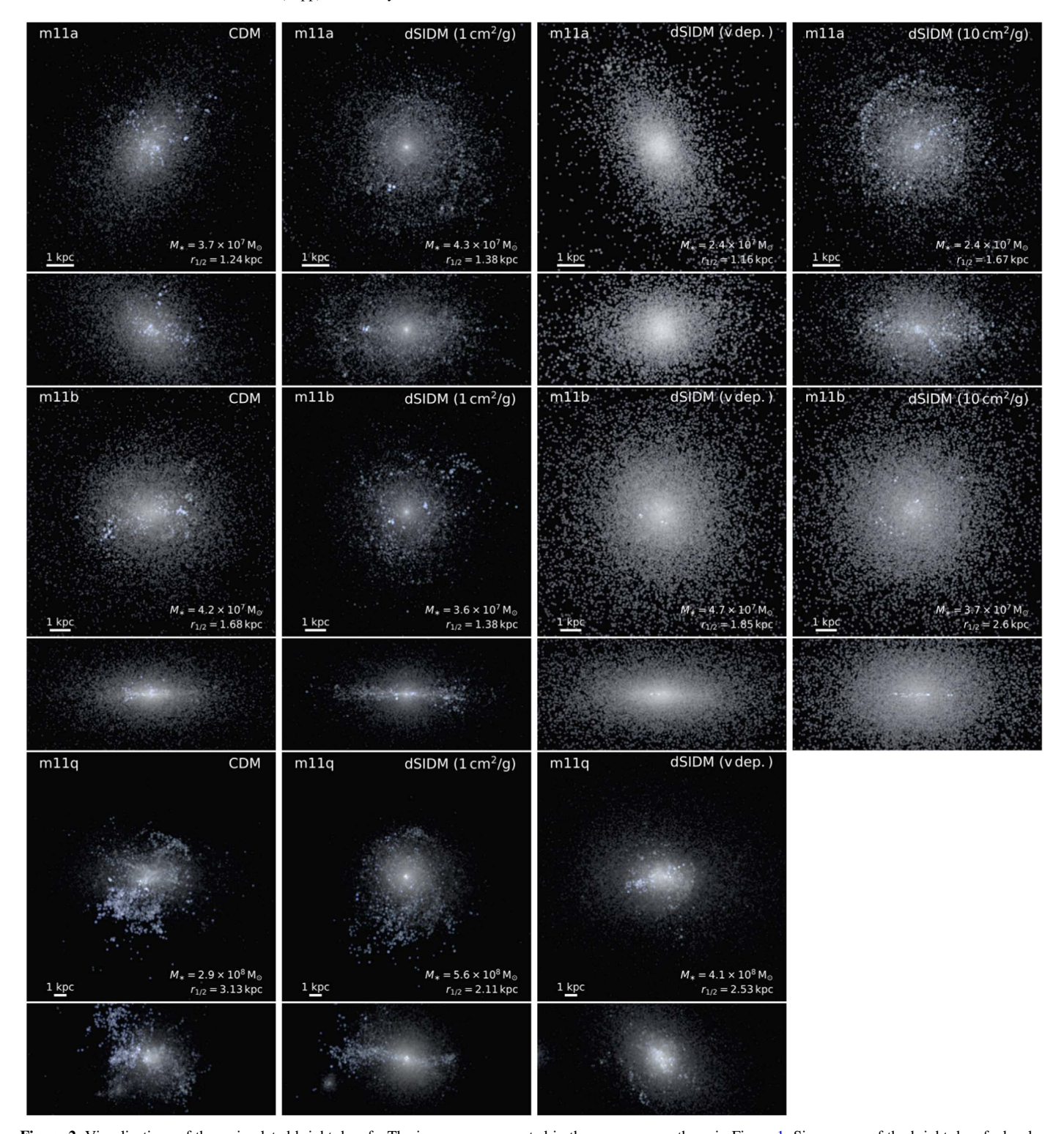


Figure 2. Visualizations of three simulated bright dwarfs. The images are generated in the same way as those in Figure 1. Since some of the bright dwarfs develop disk-like structures, we show both face-on and edge-on images here. Compared to the CDM case, the stellar disks in the dSIDM model with $(\sigma/m) = 1 \text{ cm}^2 \text{ g}^{-1}$ are more well defined and exhibit more concentrated central regions. On the other hand, the velocity-dependent dSIDM model produces galaxies that are visibly similar to the CDM case given its small effective cross section at this mass scale $((\sigma_{\text{eff}}/m) \sim 0.01 \text{ cm}^2 \text{ g}^{-1})$. Interestingly, the model with $(\sigma/m) = 10 \text{ cm}^2 \text{ g}^{-1}$ produces stellar disks accompanied by overall fluffier stellar distribution compared to the model with $(\sigma/m) = 1 \text{ cm}^2 \text{ g}^{-1}$ and CDM.

consisting of cold neutral gas while the other two dwarfs are severely perturbed by feedback. However, in dSIDM-c1, all three dwarfs show signatures of a corotating gaseous disk, with obvious diskness in the edge-on projection and spiral arms visible in the face-on projection. Similar to what we found for

the stellar disk, the compact cusps of dSIDM halos provide stronger central attraction forces to stabilize and promote the formation of thin gaseous disks. The role of modified gravitational potential/acceleration on disk formation in dwarf galaxies is studied in detail in Hopkins et al. (2023a).

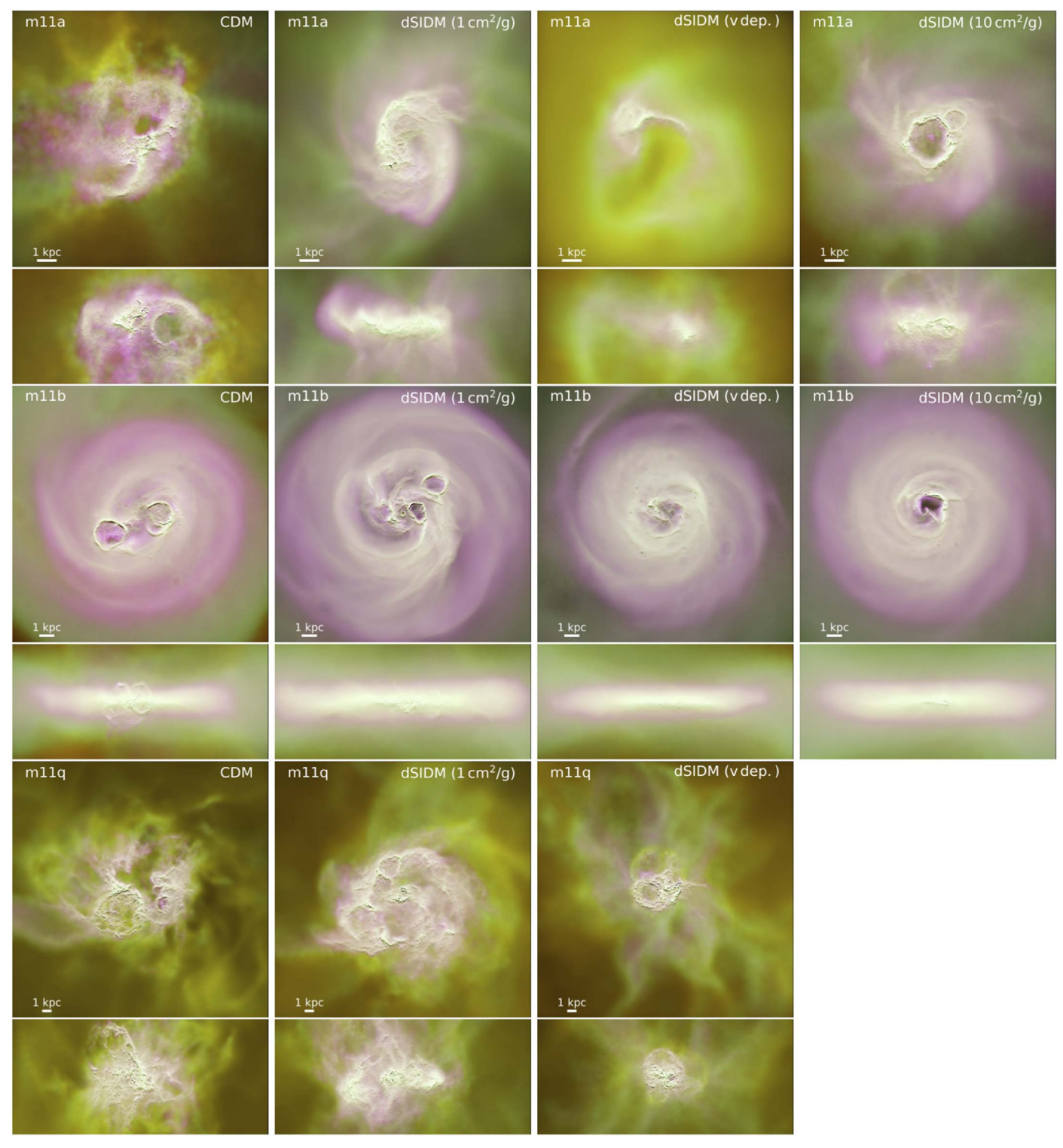


Figure 3. Visualization of the gas content of three simulated bright dwarfs. The images are logarithmically weighted gas surface density projections. Each column corresponds to one dark matter model studied, and each row corresponds to one bright dwarf simulated. For each dwarf, both the face-on and edge-on images are shown. The side lengths of the images are chosen as $12 \times r_{1/2}^{\text{cdm}}$. Each image is a composite of the gas distribution in three phases characterized by the gas temperature. The magenta color represents the *cold* neutral gas with $T \lesssim 8000$ K; the green color represents the *warm* gas with $T \sim 1-3 \times 10^4$ K; the red color represents the *hot* ionized gas in the CGM with $T \gtrsim 10^5$ K. The neutral gas disks are promoted in the dSIDM-c1 and c10 models, even in m11a, which is strongly perturbed by supernovae feedback in CDM.

3.2. Stellar Density Profiles and SFH

In Figures 4 and 5, we show the stellar density profiles of simulated classical and bright dwarfs, respectively. Each stellar density profile plot is paired with the plot of the archaeological

SFH of the galaxy. The SFH is computed as the age distribution of stellar particles selected at $r \le 0.1 \, R_{\rm vir}$ at z = 0, which is consistent with the aperture choice of our stellar mass measurements. The time bin of measuring star formation rate is

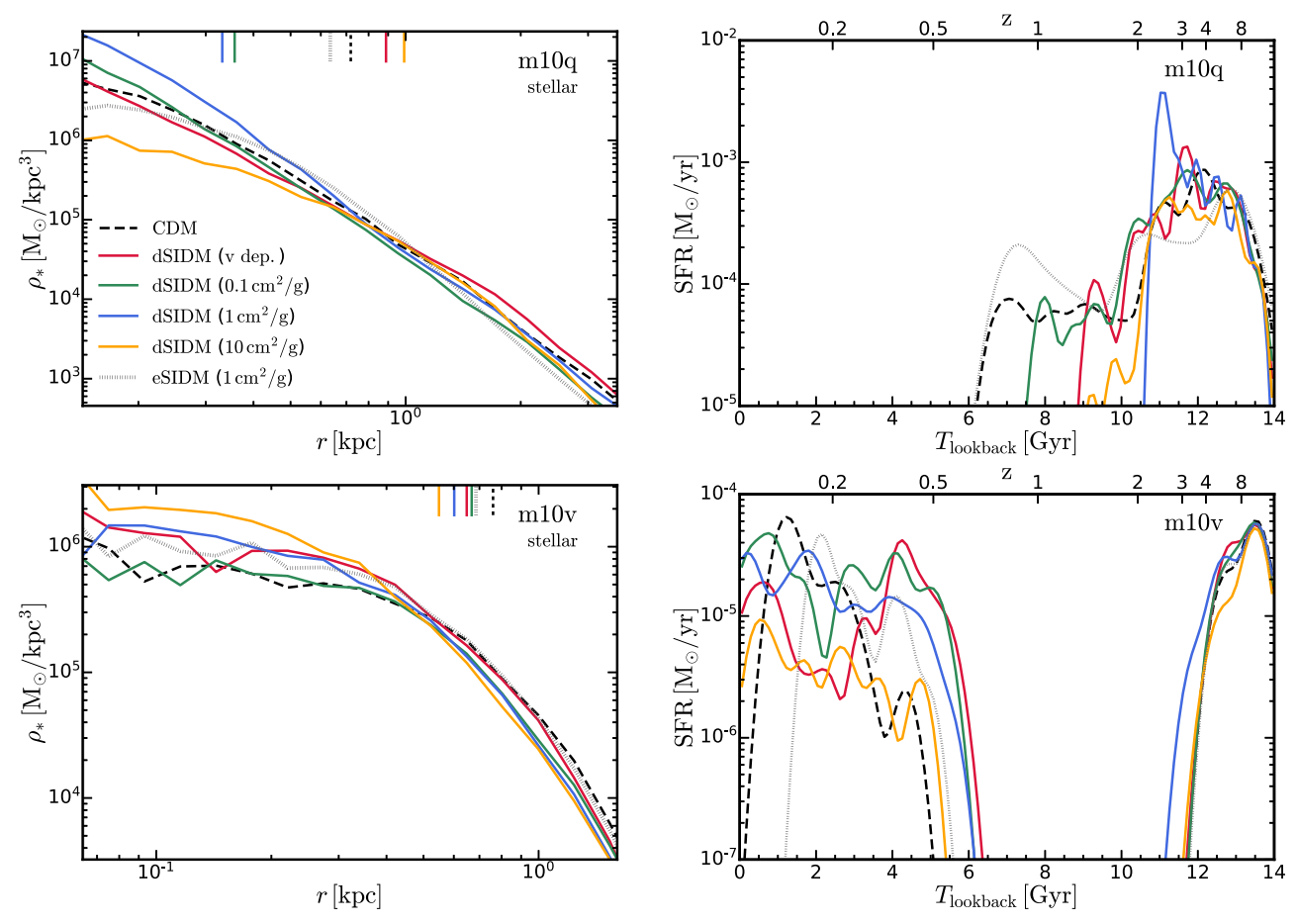


Figure 4. Left column: Stellar density profiles of simulated classical dwarfs. The density profiles from different dark matter models are presented as labeled. The short vertical lines at the top indicate the stellar-half-mass-radius of the galaxy in each model. The m10q and m10v halos show different responses to dark matter dissipation. In m10q (top), which forms its stars early, a cuspy stellar profile appears with moderate dSIDM cross sections accompanied by shrinking galaxy size, and then, the profile turns shallower when the cross section further increases. In m10v (bottom), which forms quite late, the profile becomes more concentrated monotonically as the cross section increases, and the decline of galaxy size is less dramatic. This is related to the distinct SFHs of the two galaxies as shown on the right. Right column: Archaeological SFH of simulated classical dwarfs. The galaxy m10q has an early SFH peaked at $z \simeq 3$. The stars have more time to react to the underlying dark matter distribution. On the other hand, the galaxy m10v with a relatively late period of star formation does not exhibit this. The late-time star formation and feedback also puff up the stellar content and make it less dependent on the underlying dark matter distribution.

chosen to be 100 Myr. Both in situ and ex situ star formation are counted here. In both classical and bright dwarfs, dSIDM with moderate cross sections give rise to central stellar density profiles that are cuspier than the NFW profile, and the galaxy stellar-half-mass-radii decrease correspondingly. These phenomena are likely caused by the more concentrated dark matter content in these dSIDM models. Similarly, the stellar profiles in eSIDM are cored due to the gravitational impact of thermalized dark matter cores. In the dSIDM-c10 model, the stellar distribution becomes cored and more extended, which is also related to the decreased normalization of dark matter density profiles in this model. Specifically, in Paper I, coherent rotation of dark matter was found in dissipative models with large selfinteraction cross sections (i.e., dSIDM-c10), and we showed that this drives halo deformation to oblate shapes. This combination of rotational support and change in shape leads to a decline in the central spherically measured dark matter density, which we see here is reflected in the stellar distribution.

In general, the compactness of the dark matter distribution appears to strongly influence the stellar density profile of dwarf galaxies. The star formation efficiency is regulated by the competition between feedback-driven ejection versus the

gravitational attraction from dark matter (e.g., Grudić et al. 2020). In equilibrium states (or after numerous cycles of star formation events), star formation is promoted (inhibited) in compact (diffuse) dark matter halos. The stars formed before their dark matter halo is structurally modified (e.g., before a dark disky structure or a strong cusp owing to dissipation can form) can still relax with respect to the modified halo potential within a few dynamical timescales.

One galaxy in this suite that deviates from the picture above is the classical dwarf m10v. In all dark matter models for this particular galaxy, cored stellar density profiles are developed at the galaxy center, while the central stellar density increases monotonously with dSIDM cross section. The unique stellar content of m10v could be a result of its distinct SFH (bottom right panel of Figure 4), which is dominated by several recent (very low-redshift) starburst events. The system has therefore not yet relaxed from the perturbations of the recent star formation and feedback.

In terms of the SFH, as shown in Figure 4, m10q is clearly an early forming dwarf with most of the star formation taking place at $z \gtrsim 2$ and a tail extended to $z \sim 0.7$. This is a typical SFH of isolated dwarf galaxies with $M_* \sim 10^{5-6} M_{\odot}$ in the FIRE-2 simulations (e.g., Fitts et al. 2017; Garrison-Kimmel et al. 2019b)

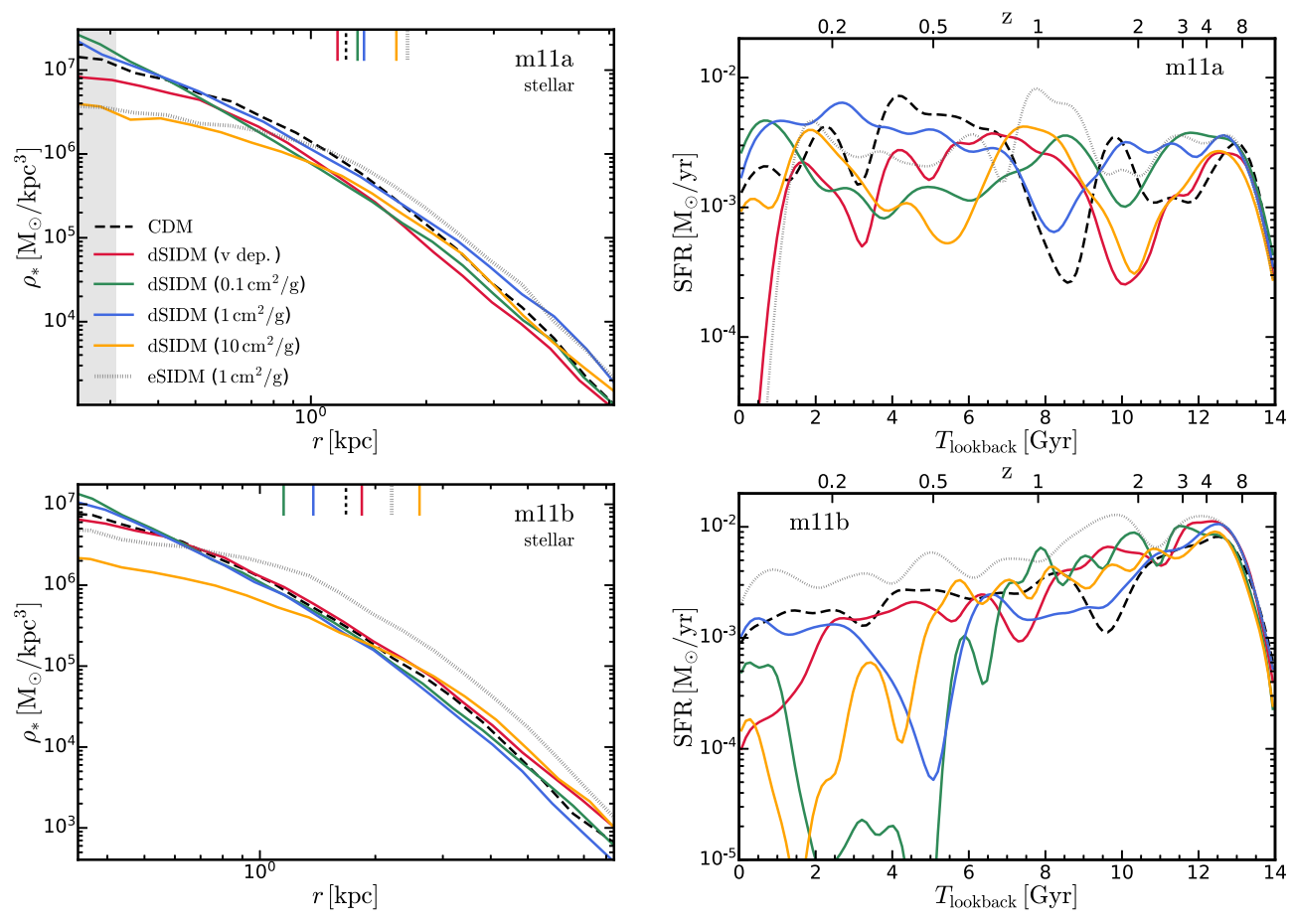


Figure 5. Left column: Stellar density profiles of simulated bright dwarfs. The notation is the same as Figure 4. The vertical shaded region indicates the convergence radius of dark matter, $r_{\rm dm}^{\rm conv}$, listed in Table 1 (for m11b and m10q,v in Figure 4, $r_{\rm dm}^{\rm conv}$ is smaller than the lower limit of the plotting range). In both m11a and m11b, the stellar density profiles become cuspy in dSIDM models with moderate cross sections while turning shallower as we further increase the cross section. This largely reflects similar behavior seen in the dark matter density profiles in Paper I—in particular, at very high cross sections, the central dark matter profiles are flattened via dark rotation. Right column: Archaeological SFHs of simulated bright dwarfs. The notation is the same as Figure 4. The galaxy m11a has a relatively flat SFH and is not significantly affected by dark matter physics. However, in m11b, dips in SFH at low redshifts appear in dSIDM models.

where star formation is halted by reionization. The gravitational potentials of low-mass halos are not sufficient to bind gas heated by the UV background radiation field in the postreionization era. However, substantial diversity exists in SFHs of dwarf galaxies (Garrison-Kimmel et al. 2019b), and some of them can experience reignition of star formation due to interactions with streams of gas in the intergalactic medium (Wright et al. 2019), which is similar to what we see in m10v. In dSIDM models with increasing effective cross sections, this tail of star formation ceases earlier, which is likely due to the faster depletion of star-forming gas in the more compact dSIDM halos. In m10v, despite drastically different SFH from m10q, the recent period of star formation also takes place earlier in dSIDM runs.

On the other hand, for the bright dwarfs shown in Figure 5, we do not see an apparent shift in the halt/onset of star formation. The SFHs of these dwarfs are continuous but fairly bursty in all the models. In m11a, the SFHs in different dark matter models do not exhibit significant differences. However, the SFH of m11b shows apparent dips at low redshifts ($z \lesssim 0.5$) in dSIDM models, which never occur in CDM or eSIDM runs. This again could be related to the faster depletion of star-forming gas in deeper gravitational potentials of dSIDM halos.

3.3. Galaxy Size-Mass Relation

In Figure 6, we compare the stellar-half-mass-radii (as a function of stellar mass) of simulated dwarf galaxies (isolated ones only; do not include satellites of Milky Way-mass hosts) with observations of dwarf galaxies in the local Universe. These observations include the Local Group dwarf spheroidal galaxies (dSphs) compiled in McConnachie (2012), dwarf galaxies from the Next Generation Fornax Survey (NGFS; Eigenthaler et al. 2018), galaxies measured in the Spitzer Photometry and Accurate Rotation Curves (SPARC; Lelli et al. 2016a, 2016b) project, and the UDGs in the Coma and Virgo cluster from van Dokkum et al. (2015), Mihos et al. (2015). The quoted effective radius (half-light radius) in the literature has been converted to the half-mass-radius assuming $r_{1/2} \simeq 4/3 R_{\rm eff}$ (Wolf et al. 2010). The purple solid line shows the galaxy size-mass relation of "normal" late-type galaxies (LTGs; Lange et al. 2015) and its extrapolation (purple dashed line) while the red solid line shows that of early-type galaxies (ETGs; van der Wel et al. 2014).

In general, despite some random galaxy-to-galaxy variations, the simulated dwarfs agree well with the observed dwarf population in the Local Universe, and follow the extrapolated size—mass relation of LTGs. The diversity of dwarfs is manifest

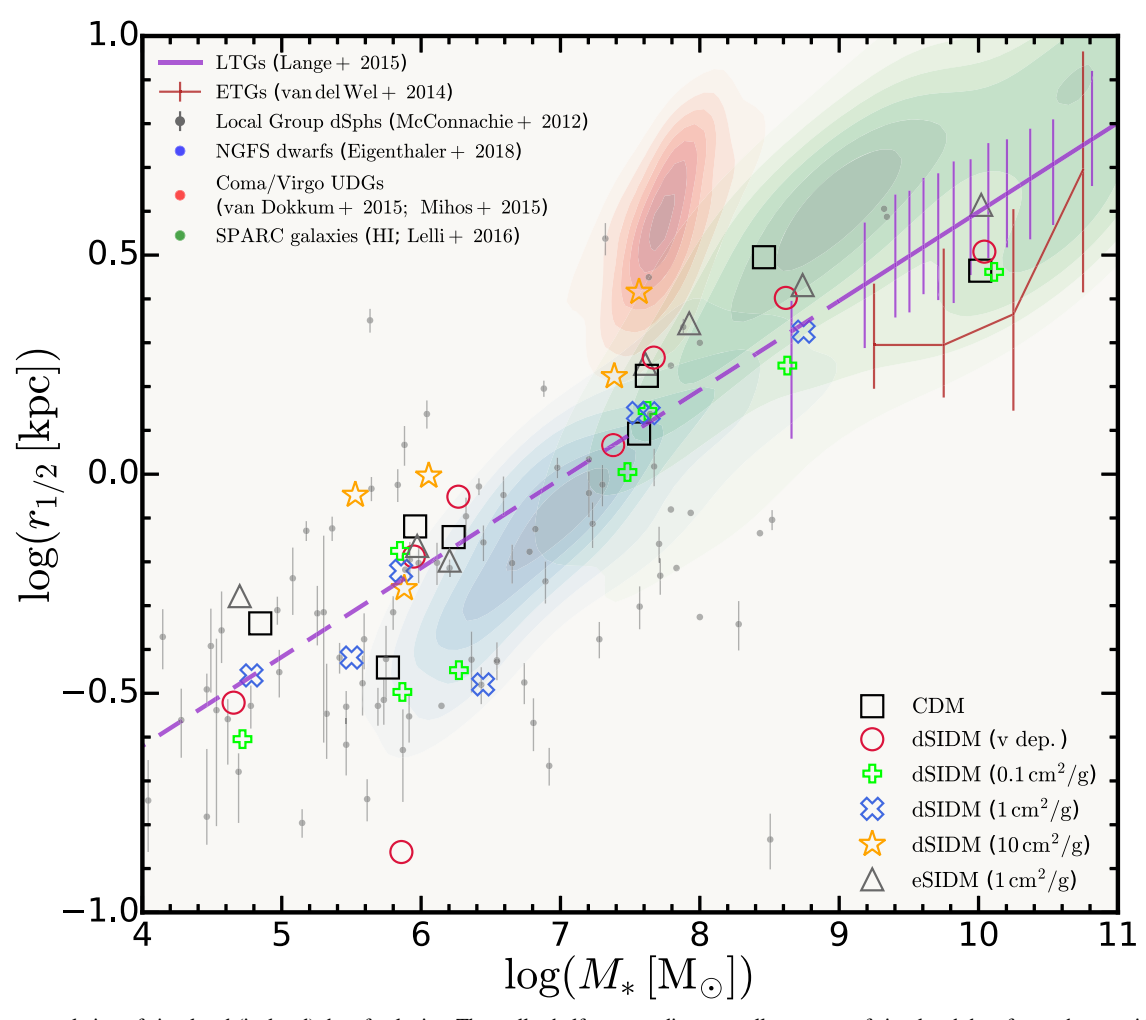


Figure 6. Size—mass relation of simulated (isolated) dwarf galaxies. The stellar-half-mass—radius vs. stellar masses of simulated dwarfs are shown with open markers (different colors correspond to different models as labeled). We compare them with several observations of dwarf galaxies in the Local Universe: gray points with error bars, the Local Group dSphs compiled in McConnachie (2012); blue contours, the NGFS dwarfs in Eigenthaler et al. (2018); green contours, the SPARC galaxies presented in Lelli et al. (2016a, 2016b); red contours, the UDGs in the Coma and Virgo cluster from van Dokkum et al. (2015), Mihos et al. (2015); purple (red) line, the size—mass relation of the observed "normal" late-type (early-type) galaxies (van der Wel et al. 2014; Lange et al. 2015). The relation of late-type galaxies is extrapolated to the $M_* \lesssim 10^9 M_{\odot}$ regime. The simulated dwarfs are consistent with the median size—mass relation of LTGs in observations and its extrapolation. With models can produce compact dwarfs at $M_* \sim 10^6 M_{\odot}$, in better agreement with Local Group observations. However, in the dSIDM-c10 model, dwarf galaxies have apparently more extended stellar content and are located at the diffuse end of the observed distribution.

as the distinction between LTGs and ETGs in massive sub-Milky Way-mass galaxies, the existence of UDGs, and the large scatter in galaxy size at $M_* \sim 10^8 M_\odot$ as well as the population of compact Local Group dwarfs that fall significantly lower than the median relation. With mild dark matter self-interaction ($(\sigma/m) \lesssim 1 \text{ cm}^2 \text{ g}^{-1}$), galaxy sizes and masses in dSIDM or eSIDM do not vary much from the CDM case. This is consistent with previous FIRE-2 studies of dwarf galaxies in eSIDM (Robles et al. 2017; Fitts et al. 2019).

Some compact dwarfs at $M_* \lesssim 10^7 M_{\odot}$ are found in dSIDM models, which are in better agreement with the observed compact dwarfs in the Local Group. However, the compact dwarf elliptical galaxies with large stellar masses $(M_* \gtrsim 10^7 M_{\odot})$ in the Local Group (e.g., Tollerud et al. 2014; Garrison-Kimmel et al. 2019a) are still hard to produce in these isolated dwarf simulations, no matter which dark matter model is employed. This point will be revisited when we study the satellite galaxies of simulated Milky Way—mass hosts. Notably in the dSIDM-c10 model, simulated dwarfs exhibit systematically more extended stellar content and shift from the median

relation. In this model, the bright dwarfs become more like analogs to UDGs, and the classical dwarfs are located at the diffuse end of the observed distribution. The dSIDM-c10 model is therefore perhaps disfavored due to this systematic shift. However, we caution that, as many of the observational studies above have noted, there could well exist a substantial population of even-lower-surface-brightness galaxies in nature, which would simply not be detected given the present state-of-the-art surface-brightness limits (see Wheeler et al. 2019). The number of dwarfs in the simulation suite is too limited to tell if dSIDM with lower cross sections are ruled out or are more consistent with the observed sample (in terms of the diversity of the stellar content).

4. Galaxy Circular Velocity Profiles

In this section, we will compare the circular velocity profiles of the simulated dwarfs with observations and attempt to derive constraints for dSIDM. Given the limited statistical sample of simulated galaxies in our study, a formal Bayesian analysis of constraints is not feasible. Consequently, we advise readers to interpret these constraints as tentative. First, we will analyze the isolated dwarfs (main *target* halos in the simulations). The ideal observational counterparts for the simulated classical dwarfs (m10 galaxies; see Table 1) are the observed field dwarfs in the Local Group (with distances to the Milky Way and M31 $d > 300 \,\mathrm{kpc}$). These field dwarfs typically have subkiloparsec $r_{1/2}$ and $M_* \lesssim 10^7 M_{\odot}$, which are comparable to the m10 galaxies. The observational counterparts for the simulated bright dwarfs (m11 galaxies) are the LSBs in the Local Universe, usually with $r_{1/2}$ of several kiloparsec and $10^7 M_{\odot} \lesssim M_* \lesssim 10^9 M_{\odot}$. In addition to the isolated dwarfs, we will analyze the subhalos (and the satellite galaxies they host) of the simulated Milky Way-mass hosts (m12 galaxies) and compare them to the observed satellites of the Milky Way and M31.

4.1. Observational Samples

For satellite galaxies, we adopt the Milky Way and M31 satellites compiled in Garrison-Kimmel et al. (2019a), which was updated based on the McConnachie (2012) compilation. These dwarf galaxies were classified as satellites with their distances to the Milky Way or M31 smaller than 300 kpc (following the criterion adopted in Wetzel et al. 2016; Garrison-Kimmel et al. 2019a). For the Milky Way satellites, this compilation includes the dSphs presented in Wolf et al. (2010), and the implied circular velocity at the 3D (deprojected) half-mass-radius, $V_{1/2} = V_{\text{circ}}(r_{1/2})$, has been calculated using their formula based on the average velocity dispersion of stars. In addition, the H I-based circular velocity measurement of the Small Magellanic Cloud from Stanimirović et al. (2004) and the proper-motion-based circular velocity measurement of the LMC from van der Marel & Kallivayalil (2014) are included in this compilation. For the satellites of M31, the compilation included the $r_{1/2}$ and $V_{1/2}$ measurements from Tollerud et al. (2014). For the dwarfs in the Local Field (with distances to hosts larger than 300 kpc), the compilation included the $r_{1/2}$, $V_{1/2}$, and σ_{v*} , from Kirby et al. (2014) where possible, although with modifications to the three galaxies with evidence of rotation (Garrison-Kimmel et al. 2014). In total, there are 12, 31, 13 dwarf galaxies included for the Milky Way, M31, and Local Field, respectively. A recent measurement (Taibi et al. 2020) on the field dwarf "Tucana" obtained a much lower dynamical mass of the system than the previous measurements (Fraternali et al. 2009; Gregory et al. 2019), so we update the compilation correspondingly.

For the LSBs, we adopt the H I rotation curves and mass models from the "Local Irregulars That Trace Luminosity Extremes, The H I Nearby Galaxy Survey" (LITTLE THINGS; Oh et al. 2015). The mass modeling results in Oh et al. (2015) showed that the selected galaxies have a typical halo mass of $\sim 10^{10-11} M_{\odot}$ and stellar mass of $\sim 10^{7-9} M_{\odot}$, which are in good agreement with the simulated bright dwarfs. In addition, we include the H I/H α rotation curves and mass models from the SPARC project (Lelli et al. 2016b). In total, there are rotation curves of 30 (175) dwarfs in the LITTLE THINGS (SPARC) sample. Given the limited statistics provided by only three simulated bright dwarfs, we will do a case-by-case comparison by selecting observed galaxies based on their maximum circular velocities, effective radii, and inferred stellar masses.

4.2. Circular Velocity Profiles of Isolated Dwarfs

In the top left panel of Figure 7, we show the circular velocity profiles of the simulated classical dwarfs in different dark matter models. In general, the circular velocities at $r \lesssim 1$ kpc increase in dSIDM models with effective cross section 13 0.1 cm 2 g $^{-1} \lesssim (\sigma/m)_{\rm eff} \lesssim 1$ cm 2 g $^{-1}$, and the circular velocity profiles are almost flat at the center. For example, the circular velocities at $r \simeq 0.2$ kpc are enhanced by about a factor of 2 in the dSIDM-c1 model compared to those in the CDM case. This is a direct consequence of the cuspy central density profiles in dSIDM models, as detailed in Paper I. In the dSIDM-c10 model, circular velocity profiles have similar flat shapes but with systematically lower normalizations than those in the dSIDM-c1 model, which is likely related to the coherent rotation and halo deformation in the strong dissipation limit.

In the other three panels of Figure 7, we show specifically the $(V_{1/2}, r_{1/2})$ values of the simulated dwarfs and compare them to the circular velocities of 10 observed Local Group field dwarfs (compiled in Section 4.1). For Tucana, both the recent measurement (Taibi et al. 2020), which attempts to subtract a potential correction (still somewhat uncertain) for unresolved stellar binaries, and an older measurement (Fraternali et al. 2009) without such a correction are shown and linked by a gray dashed line in the figure. The circular velocity profiles in CDM are consistent with the bulk of the observed dwarfs, except two dense outliers (Tucana, if we take the older measurement and NGC6822) with $V_{1/2} \sim 30-40 \, \mathrm{km \, s^{-1}}$. The dSIDM-c0.1 and dSIDM-c1 models are marginally consistent with observations: the $V_{1/2}$ of some simulated dwarfs are slightly higher than the observed dwarfs of similar $r_{1/2}$ except for NGC6822 (if we adopt the new measurement of Tucana), but the differences at this level are not enough to rule out these models given the limited statistics.

For the velocity-dependent dSIDM model, the simulated dwarfs are consistent with the relatively compact observed dwarfs but may be in tension with the six diffuse ones. Again, the limited statistics prevent us from drawing any conclusions about the model. For the dSIDM-c10 model, although the circular velocities at small radii appear higher than the observed ones, the $V_{1/2}$ are still consistent with the observed dwarfs with comparable sizes. The potential problem with this model is that the stellar content of all simulated dwarfs is relatively diffuse, and the range of galaxy stellar effective radii may not be diverse enough to match observations. We also note that there is one observed galaxy (NGC6822, or two if the older Tucana measurement is used) lying above the circular velocity profiles of any simulated galaxies regardless of the dark matter model employed. Even the model with the highest degree of dissipation used here cannot produce analogs of these compact systems. If the discrepancy is real (not the result of, e.g., unresolved binaries or other sources of dispersion), the physical origin of these systems in the field is still a challenge to existing cosmological simulations (e.g., Dutton et al. 2016; Fattahi et al. 2016; Sawala et al. 2016; Wetzel et al. 2016; Garrison-Kimmel et al. 2019a).

In the top left panel of Figure 8, we show the circular velocity profiles of the simulated bright dwarf galaxies in different dark matter models. The circular velocities in the

 $[\]overline{^{13}}$ The effective cross section $(\sigma/m)_{\rm eff}$ follows the definition in Paper I, which is equivalent to σ/m for models with constant cross sections. For the velocity-dependent model we study, the effective cross section is about $0.3~{\rm cm}^2~{\rm g}^{-1}$ at the mass scale of classical dwarfs.

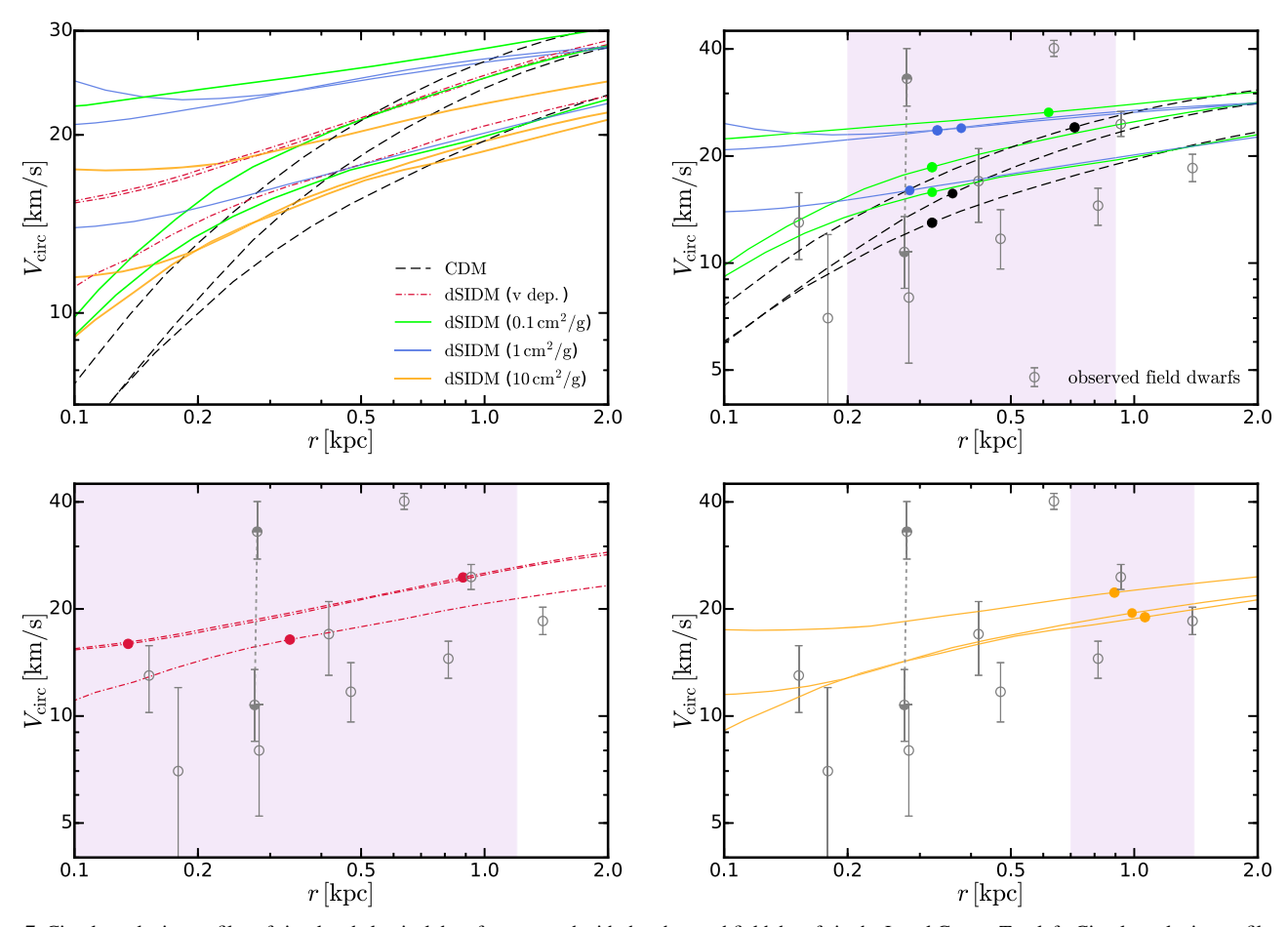


Figure 7. Circular velocity profiles of simulated classical dwarfs compared with the observed field dwarfs in the Local Group. Top left: Circular velocity profiles of the simulated dwarfs in different dark matter models (as labeled). The circular velocities are enhanced at subkiloparsec scale in dSIDM models. In the model with $(\sigma/m) = 10 \text{ cm}^2 \text{ g}^{-1}$, the normalization of the circular velocity profile decreases. Top right: We compare the results in CDM and dSIDM models with $(\sigma/m) = 0.1 \text{ or } 1 \text{ cm}^2 \text{ g}^{-1}$ with the observed field dwarfs in the Local Group (shown by gray open circles with error bars). For Tucana, we show two measurements connected by a gray line (see text for details). The $r_{1/2}$ of these galaxies are shown by solid circles. We highlight the observed dwarfs of similar sizes to the simulated one $(0.2 \text{ kpc} \lesssim r_{1/2} \lesssim 0.9 \text{ kpc})$ with the purple shaded region. The CDM results are consistent with the majority of the observed dwarfs, but lower compared to the most compact dwarfs (NGC6822 and the older measurement of Tucana). The $(V_{\text{circ}}(r_{1/2}), r_{1/2})$ of these two dSIDM models are still marginally consistent with the observed dwarfs of similar sizes and improve the agreement for compact dwarfs. The circular velocities in the dSIDM models are about 2 times higher than the observed ones at small radii $r \lesssim 0.2 \text{ kpc}$. Bottom left: we show the results of the velocity-dependent dSIDM model and compare them to the observed dwarfs with $0.1 \text{ kpc} \lesssim r_{1/2} \lesssim 1.2 \text{ kpc}$. Bottom right: We show the results of the model with $(\sigma/m) = 10 \text{ cm}^2 \text{ g}^{-1}$ and compare them to the observed dwarfs with $0.7 \text{ kpc} \lesssim r_{1/2} \lesssim 1.5 \text{ kpc}$. The results from these two models are also consistent with observations.

dSIDM-c0.1 and dSIDM-c1 models are enhanced to about 30–40 km s⁻¹ at $r \lesssim 1$ kpc. The circular velocity profiles in the dSIDM-c10 model have similar shapes but lower normalizations. Those in the velocity-dependent dSIDM model are almost indistinguishable from the CDM case, due to the limited effective cross sections in the bright dwarfs. In the other three panels, we compare the circular velocity profiles of each simulated dwarf with the HI-based measurements from the LITTLE THINGS survey (Oh et al. 2015) and the SPARC survey (Lelli et al. 2016b) as introduced in Section 4.1. For m11a, we select observed galaxies with maximum circular we select observed galaxies with maximum velocities $40 \text{ km s}^{-1} \lesssim V_{\text{circ}}^{\text{max}} \lesssim 60 \text{ km s}^{-1}$, and, for m11b, we select observed galaxies with $50 \text{ km s}^{-1} \lesssim V_{\text{circ}}^{\text{max}} \lesssim 70 \text{ km s}^{-1}$. In addition, for both galaxies, we require the observed sample to have $0.5 \,\mathrm{kpc} \lesssim r_{1/2} \lesssim 3 \,\mathrm{kpc}$ and $10^7 M_{\odot} \lesssim M_* \lesssim 10^{8.5} M_{\odot}$. From these comparisons, we find that the CDM and the velocity-dependent dSIDM model are fully consistent with observations at these mass scales. However, the circular velocities in the dSIDM-c0.1 and dSIDM-c1 models are about 2 times higher than the observed values at the subkiloparsec scale, and the discrepancy appears to be larger than both the

observational uncertainties as well as the galaxy-to-galaxy scatter.

For the massive dwarf m11q, we select observed galaxies with $60~{\rm km~s^{-1}} \lesssim V_{\rm circ}^{\rm max} \lesssim 80~{\rm km~s^{-1}}$, $1~{\rm kpc} \lesssim r_{1/2} \lesssim 5~{\rm kpc}$, and $10^8 M_{\odot} \lesssim M_* \lesssim 10^9 M_{\odot}$. The CDM and the velocity-dependent dSIDM models are again consistent with the median circular velocity profiles of the observed dwarfs. However, due to the prominent diversity of the observed circular velocity profiles at the mass scale, the dSIDM-c0.1 and dSIDM-c1 models are still marginally consistent with observations.

In conclusion, the comparisons of the three bright dwarfs with observations appear to disfavor both of the constant cross-sectional dSIDM models with $(\sigma/m) \gtrsim 0.1 \, \mathrm{cm^2 \, g^{-1}}$. However, a velocity-dependent model is still viable to produce unique phenomena in lower-mass dwarfs while maintaining consistency with the H I-based observations of bright dwarfs.

One important caveat we note is that the measurements here all adopt HI as the kinematic tracer of the gravitational potential. This certainly involves an additional layer of uncertainties in fitting the HI velocity field and asymmetric drift corrections. In addition, the galaxies selected in the

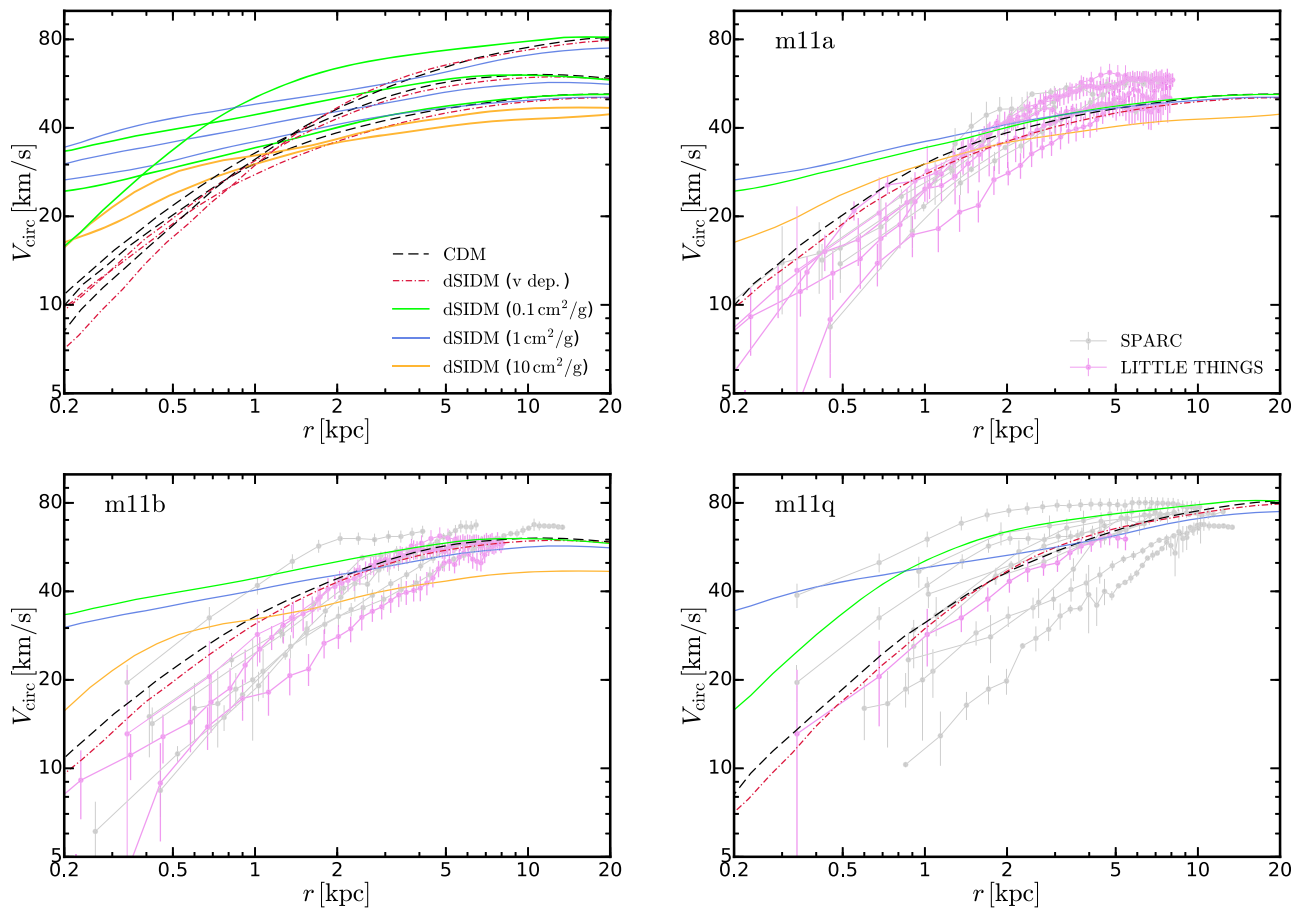


Figure 8. Circular velocity profiles of simulated bright dwarfs compared with observed LSBs in the Local Universe. Top left: circular velocity profiles of the bright dwarf galaxies in simulations with different dark matter models (as labeled). Top right and bottom panels: We compare the results with the measured circular velocities of LSBs observed in the field shown by gray and purple lines with error bars (see Section 4 for details of the observed sample and selection criteria). Models with constant σ/m that are consistent with the classical dwarfs (i.e., with low $V_{\rm circ}^{\rm max}$) generally produce too concentrated galaxies at high $V_{\rm circ}^{\rm max}$, but the velocity-dependent model is consistent over the entire range we consider here.

observational sample all are chosen to exhibit cold dense gas disks. Most galaxies so selected are morphologically spiral or irregular galaxies, and the observed samples by construction will miss elliptical or spheroidal dwarf galaxies lacking a dense HI disk, which some authors have argued may be more compact than the late-type disky galaxies of similar stellar masses (e.g., van der Wel et al. 2014; Eigenthaler et al. 2018). This could potentially bias the comparison here and naively might loosen the constraints on dSIDM models. However, as shown in Figure 3, disk-like structures of cold neutral gas are indeed prominent in m11a and m11b and are promoted in dSIDM models. Therefore, compared to the CDM case, the galaxies in dSIDM models would be more likely to appear in HI selected samples in observations, but actually match less well with the measured circular velocity profiles of those samples.

4.3. Circular Velocity Profiles of Satellites of Milky Way–Mass Hosts

The comparisons above focus on isolated systems to avoid contamination with environmental effects, but the derived tentative constraints are subject to galaxy-to-galaxy statistical variations given the limited number of isolated dwarfs in the simulation suite. An alternative way to constrain the dSIDM models is to compare satellite galaxies of more massive hosts to

improve the statistics. For this purpose, we analyze the three low-resolution (l.r.) runs of Milky Way-mass hosts (m12i, m12m, and m12f) and an h.r. run for m12i (details listed in Table 1). Their subhalos (as well as the associated stellar content) are identified with the procedure introduced in Section 2.3.

In Figure 9, we show the circular velocity profiles of satellite galaxies of simulated Milky Way–mass galaxies (the median curve, the 1.5σ scatter, and the three satellites with the maximum/minimum rotation velocities at r=1 kpc) and compare them with the observed satellites of the Milky Way and M31 compiled in Garrison-Kimmel et al. (2019a) as introduced in Section 4.1. For simulations, the identified subhalos are classified as *satellites* if their distance from the center of the Milky Way or M31-analog is $20 \text{ kpc} \le d \le 300 \text{ kpc}$. We only keep satellites with dark matter particle number $N_{\text{dm}} \ge 200$ and associated stellar particle number $N_* \ge 10$, which roughly corresponds to a stellar-mass cut of $M_* \ge 7 \times 10^4 (5.6 \times 10^5) M_{\odot}$ for high-(low-)resolution simulations. For reference, the minimum stellar mass of the observed sample we select is $7.3 \times 10^4 M_{\odot}$ ($3 \times 10^5 M_{\odot}$) for M31 (Milky Way).

As shown in Figure 9, the circular velocities in dSIDM models are slightly higher than their CDM counterparts (both the median and upper scatter), but the differences are subdominant compared to the intrinsic scatter of the observed

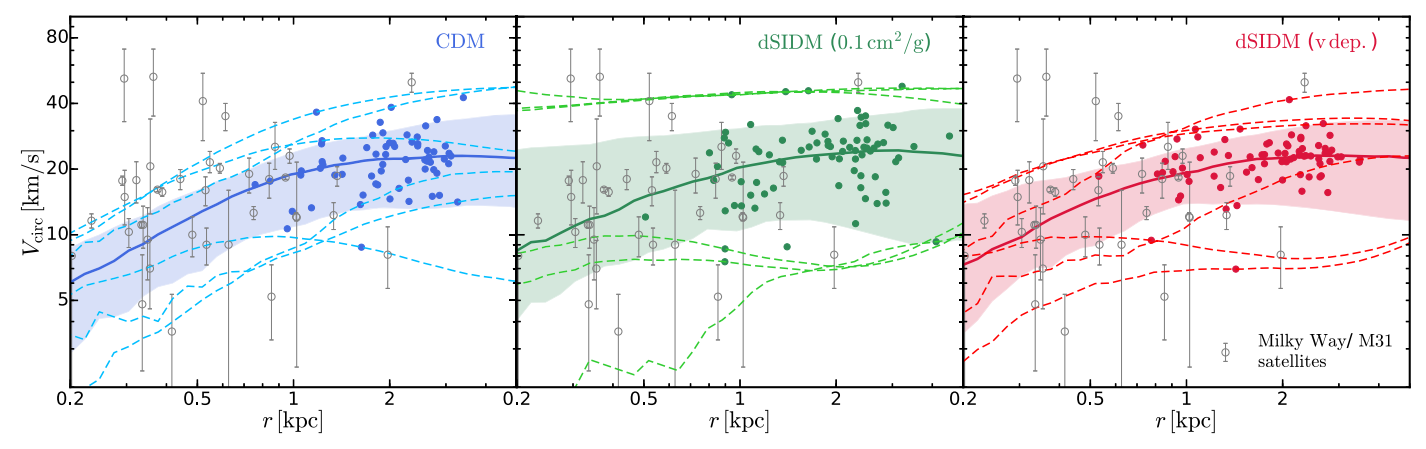


Figure 9. Circular velocity profiles of satellite galaxies of simulated Milky Way-mass galaxies and compared with observations. The circular velocity profiles in each dark matter model are shown in each column respectively. The solid lines and the shaded regions show the median and the 1.5σ scatter (86% of the sample) of the curves. The dashed lines highlight the three circular velocity profiles with the highest (and the three with the lowest) circular velocities at r = 1 kpc. Gray circles with error bars show the $(V_{1/2}, r_{1/2})$ of observed Milky Way and M31 satellites compiled in Section 4.1. The $r_{1/2}$ values of simulated satellites are marked by solid circles. According to Section 2.3, the selected satellites from simulations are in the mass range $M_* \sim 10^5 - 10^8 M_{\odot}$, in concordance with the observed sample. The circular velocity profiles in different models are almost indistinguishable compared to the scatter among the observed satellites, despite the slightly larger median rotation velocities and higher scatter in the dSIDM-c0.1 model. Circular velocity profiles from all three models are consistent with the bulk of the observed dwarfs, although the predicted galaxy sizes are systematically larger. The smallest $r_{1/2}$ reached in the two dSIDM models is smaller than that from the CDM case, down to about \sim 500 pc. As indicated by the dashed lines, the most compact satellites in the dSIDM-c0.1 model agree better with the observed compact dwarfs in the Local Group; though, the stellar content is still puffier compared to observations.

satellites. Despite the fact that the circular velocity profiles in all the models are consistent with the majority of the observed dwarfs, the stellar-half-mass-radii are systematically larger than the observed values. This will be discussed in more detail in the comparison of the size-mass relation below. In addition, the CDM and the velocity-dependent dSIDM model fail to produce the most compact dwarf with $r_{1/2} \lesssim 1 \,\mathrm{kpc}$ and $V_{1/2} \sim 40 \,\mathrm{km \, s^{-1}}$, which are typically elliptical or irregular galaxies in the M31 subgroup with stellar masses $\gtrsim 10^8 M_{\odot}$. However, the dSIDM-c0.1 model gives a larger scatter in the rotation velocities at the subkiloparsec scale and can produce analogs of those galaxies. But we need to note that the presence of compact satellite analogs in the dSIDM run (while not in CDM) needs further validation with the improved statistics of the host systems simulated (at this point, it is difficult to say how significant the result is). It is worth mentioning that the difference is smaller compared to isolated halos. This could be caused by heating from various environmental effects, e.g., evaporation and tidal heating balancing the cooling of dark matter and suppressing cusp formation (e.g., Zeng et al. 2022).

The typical mass and size of the satellites studied here are similar to the isolated classical dwarfs studied in Section 4.2. However, the differences between the dark matter models found in these satellites are smaller than what we found for field dwarfs. First, this could be related to additional factors that affect galaxy structure in a group environment, such as dynamical friction, tidal and ram pressure stripping (e.g., Quinn & Goodman 1986; Colpi et al. 1999; Taylor & Babul 2001; Zentner & Bullock 2003; Gan et al. 2010; Jiang & van den Bosch 2016). But a more plausible explanation would be the resolution effects. The Milky Way-mass host simulations are about 30 times poorer in mass resolution (i.e., $m_b = 7000 M_{\odot}$ for m12i versus $250M_{\odot}$ for m10q) than the isolated dwarf simulations. Since the impact of dSIDM typically shows up at very small radii $r \lesssim 500$ pc, this could be challenging to resolve in $m_b = 7000 M_{\odot}$ runs (see the convergence plots of m10q and m10v in Hopkins et al. 2018).

In Figure 10, we show the size–mass relation for selected satellite galaxies from simulations and compare them to observations. The Local Group dSphs and the NGFS dwarfs compiled for Figure 6 are shown here again for reference. Similar to what we did in Section 3.3, the quoted effective radius in the literature has been converted to the half-mass-radius assuming $r_{1/2} \simeq 4/3 R_{\rm eff}$ (Wolf et al. 2010).

The galaxy size measurements are often affected by the surface-brightness detection limit in observations. Following Wheeler et al. (2019), this is estimated to be $\mu_{\rm V}=30~{\rm mag~arcsec^{-2}}$ for SDSS, which corresponds to a physical stellar surface density limit $\Sigma_*^{\rm lim}=0.036M_\odot~{\rm pc^{-2}}$ assuming solar absolute magnitude $M_{\odot,{\rm V}}=4.83$ and a stellar mass-to-light ratio of $M_*/L\simeq 1M_\odot/L_\odot$. The limit is indicated with the gray dotted line in Figure 10 when $\Sigma_{1/2}\equiv M_*/\pi~r_{1/2}^2=\Sigma_*^{\rm lim}$. We also show the surface density limit with an order of magnitude increased sensitivity at $\mu_{\rm V}=32.5~{\rm mag~arcsec^{-2}}$ for future surveys.

In simulations, a significant population of low-mass satellites has a surface brightness close to or below the observational detection limit, the majority of which will not be detected in current surveys. Even the bright ones are potentially affected by the surface-brightness cut in size/mass measurements. To correct for this effect, we measure the stellar surface density profile and truncate it where the average enclosed stellar surface density drops below Σ_*^{\lim} . The stellar mass is then corrected to the enclosed stellar mass within the cutoff radius, and the $r_{1/2}$ is also corrected correspondingly. If the stellar surface density of the satellite is too low to identify the cutoff radius, the satellite is removed from the sample.

After this correction, most of the satellites eventually reside in the detectable region on the size-mass plane. However, compared to the observed satellites, they are systematically more diffuse, which is consistent with what we found in Figure 9. No obvious difference between dark matter models is found, despite the fact that the satellites at the massive end in the dSIDM-c0.1 model are more compact than the CDM

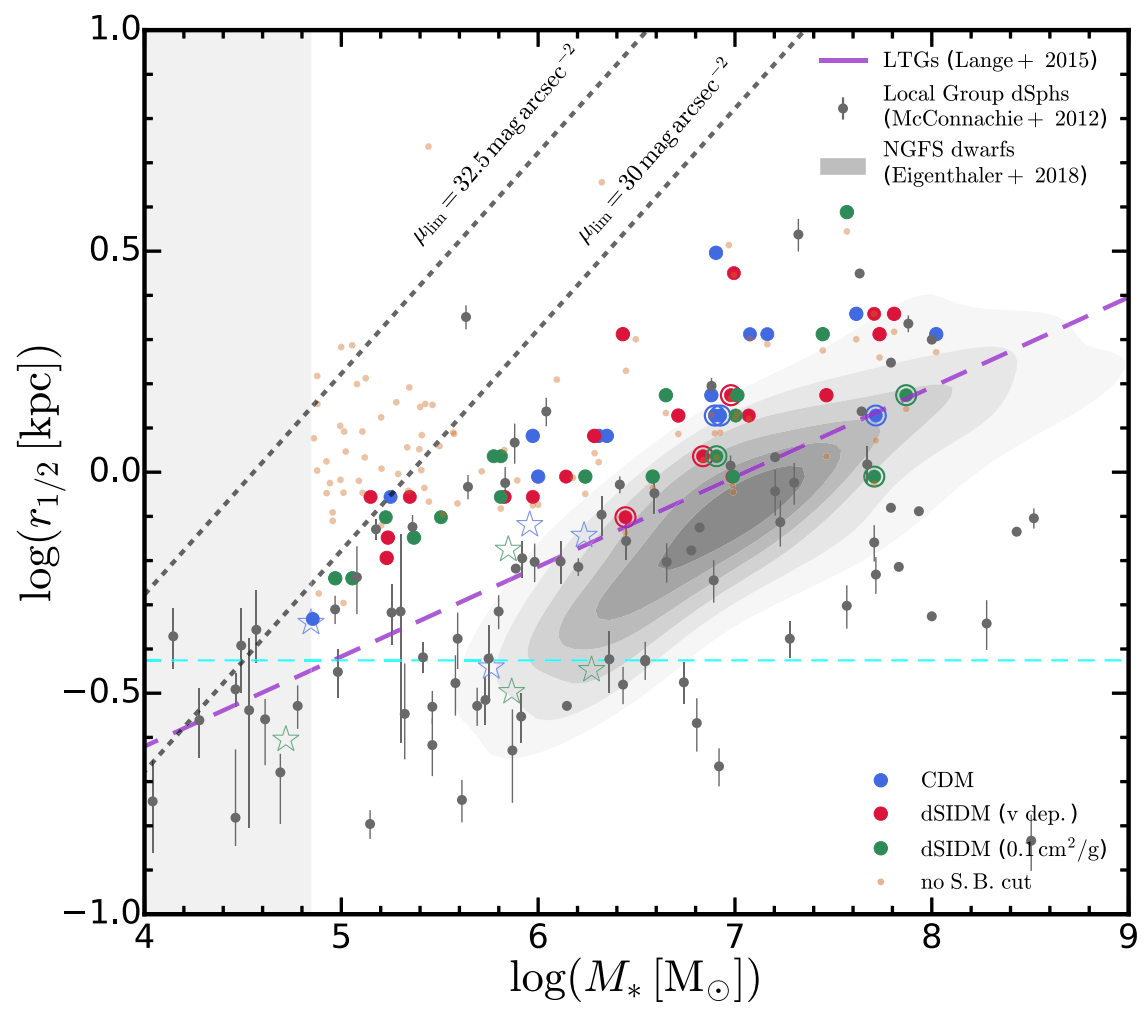


Figure 10. Size—mass relation of satellite galaxies. We show the stellar-half-mass—radius vs. stellar mass of satellites of the simulated Milky Way—mass host(s) in different models (as labeled). Only the high-resolution runs are considered here. The satellites from simulations follow the same selection criteria as in Figure 9. The large solid points show satellite sizes corrected for the surface-brightness limit in observations while the small orange points show results with no corrections. The gray dotted lines indicate the surface-brightness limit 30 mag arcsec⁻² for the SDSS surveys and the limit with an order of magnitude increased sensitivity. For reference, the Local Group dwarfs (McConnachie 2012) are shown by gray points, and the NGFS dwarfs (Eigenthaler et al. 2018) are shown by the gray shaded contours. The purple dashed line is the extrapolation of the size—mass relation of local late-type galaxies (Lange et al. 2015). The shaded region on the left indicates the mass resolution limit of the simulated satellites. The horizontal cyan dashed line indicates the radius limit where the enclosed dark matter particle number is ≤ 200 for a typical satellite central density $\rho_{\text{dm}} \simeq 10^{7.5} M_{\odot}$ kpc⁻³. The encircled markers highlight the three most compact dwarfs (with the highest rotation velocities at r = 0.5 kpc) in each run. A significant population of low-mass satellites in simulations is not detectable in current observations. For those in the observed regime, no obvious difference is found between CDM and dSIDM models. Massive satellites in dSIDM models are slightly more compact than their CDM counterparts, but they are still systematically puffer than the observed ones. In all the models, the satellites with the most compact dark matter content (highest circular velocities identified in Figure 9) also have the most compact stellar content. However, despite similar stellar masses, they have about 3 times larger $r_{1/2}$ than the observed compact dwarfs (isolated systems) are shown as op

counterparts. It is usually the satellites with the most compact dark matter content (highest circular velocities at the subkiloparsec scale) that also exhibit the most compact stellar content. In Figure 9, we found that the most compact satellites in the dSIDM-c0.1 model are better counterparts to the observed compact dwarf elliptical galaxies in the Local Group, in terms of their circular velocities.

However, in the size-mass plane, it is clear that these satellites found in simulations still do not have compact enough stellar content to match the most compact observed systems. This discrepancy could owe to observational effects (e.g., selection effects making it much easier to identify high-surface-brightness objects, or the fact that observations often use the light-weighted, Sérsic-estimated profiles rather than the mass-

weighted $r_{1/2}$ we measure here), or to the fact that some "satellites" may have their light profiles dominated by a single, massive/compact star cluster (or even themselves be a star cluster entirely rather than a true dwarf galaxy) as shown in some very h.r. simulations in Ma et al. (2018). Exploring these possibilities will require more detailed forward modeling in future work. Similar to the point we made above about the circular velocity profiles of satellites, we caution that this discrepancy could also be a resolution effect. Specifically, with about an order-of-magnitude better mass resolution, the simulated isolated dwarfs at a similar mass scale are in better agreement with the observed samples. The potential resolution effects will be discussed in detail in Appendix A.

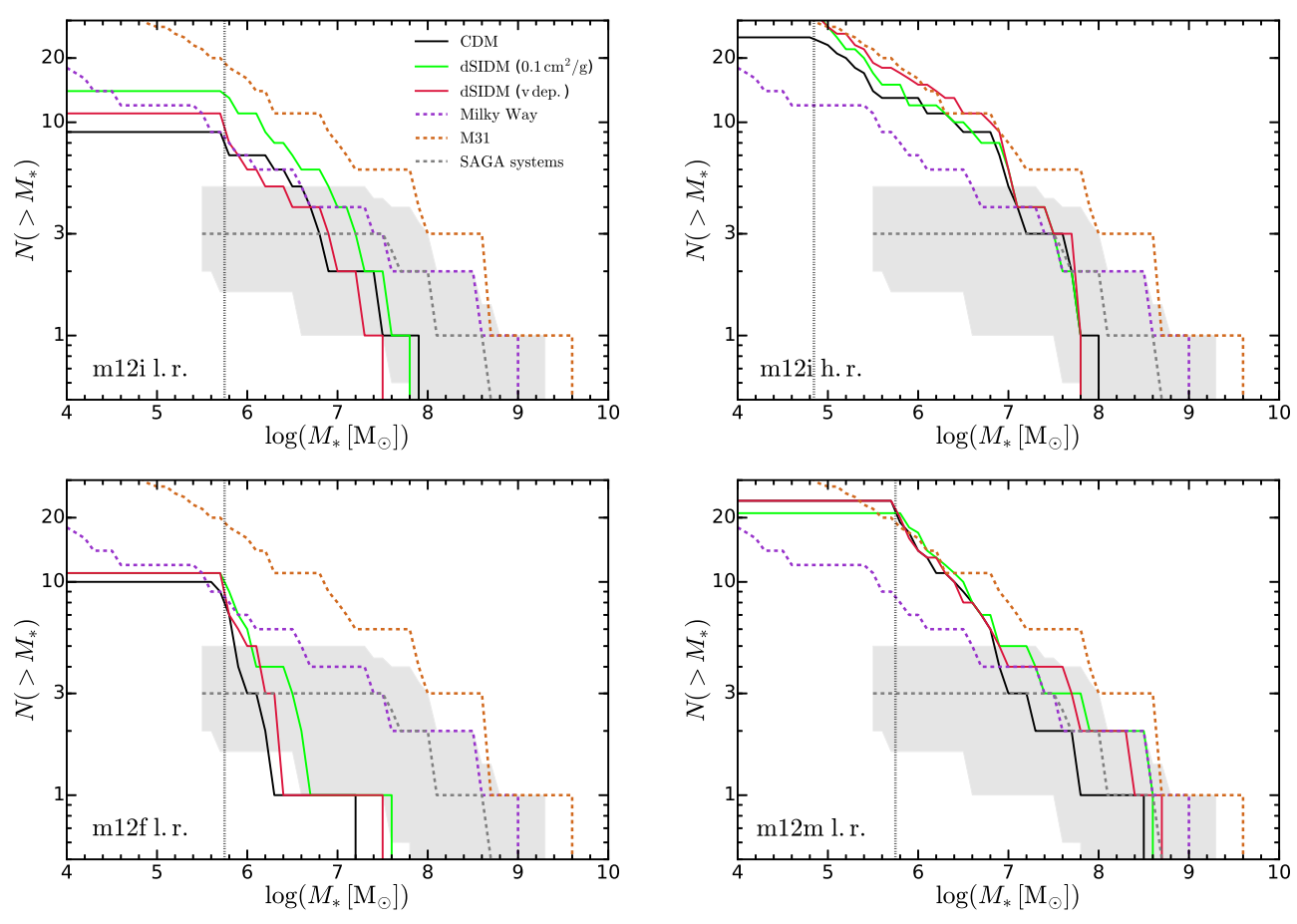


Figure 11. Cumulative satellite stellar mass function. The cumulative satellite stellar mass functions of different dark matter models are shown in solid lines with different colors (as labeled). The purple and orange dashed lines show the cumulative satellite stellar mass functions of the Milky Way and M31, respectively. The gray dashed lines with shaded regions show the mass functions of Milky Way-like systems in the SAGA survey with 1σ scatter. Each panel corresponds to one simulated Milky Way-mass galaxy in the suite. The vertical dotted line indicates the resolution limits of satellite stellar mass (set as 10 times the baryonic mass resolution of the simulation). Strong diversity shows up in the stellar mass function of both observed satellites and the satellites of simulated galaxies. The counts of satellites get enhanced slightly in the dSIDM models, but the differences are still too small compared to the observed scatter to effectively rule out any of the models studied.

5. Satellite Counts

In addition to the internal structure of satellites, the number counts of satellites could also serve as a channel to constrain alternative dark matter models. For example, the most wellknown small-scale issue is the MS problem (Klypin et al. 1999; Moore et al. 1999), which states that the dark matter subhalos around Milky Way-mass hosts in DMO simulations outnumber the observed satellites in the actual Milky Way. The problem has been alleviated by the growing number of observed satellites in the Local Group and more realistic modeling of the baryonic physics in CDM simulations (e.g., Wetzel et al. 2016; Garrison-Kimmel et al. 2019a; Samuel et al. 2020). In some cases, the observed satellite statistics and distribution can be used to constrain alternative dark matter theories. For example, Nadler et al. (2021) used observational data from the DES and Pan-STARRS1 to constrain several alternative dark matter models that suppress the linear matter power spectrum at small scales.

Specifically for SIDM, the properties of satellites can be changed in nontrivial ways. Thermalized cores generated by eSIDM can make satellites prone to tidal stripping. The ram pressure stripping resulting from self-interactions between satellite and host halo particles can drive material out of subhalos. The relative importance of ram pressure stripping can

also vary as the cross section has velocity dependence. For instance, in Nadler et al. (2020a), Banerjee et al. (2020), the evolution of the satellite preinfall and postinfall have been systematically studied for the eSIDM models with various velocity dependences. Different types of SIDM can also give rise to very different satellite responses. In Vogelsberger et al. (2019), they studied a multi-state SIDM model featuring inelastic (mainly exothermic) interactions and found that this type of interaction suppresses the abundance of substructures in Milky Way-mass halos considerably. In Fischer et al. (2022), they studied highly anisotropic dark matter self-interactions with large scattering rates but low momentum transfer efficiency per scattering. They found a larger suppression of satellite abundance in this model compared to the isotropic model. Satellite statistics and evolution in dSIDM have not yet been studied in previous works. In the regime where $t_{\rm diss} \ll t_{\rm H}$, dark cusps can develop in dwarf galaxies prior to infall, making them more resilient against tidal stripping and having higher chances to penetrate deeper in the host halo.

In Figure 11, we show the cumulative satellite stellar mass functions from simulated Milky Way-mass galaxies and compare them to the observed mass functions of the Milky Way, M31, and 36 Milky Way-like systems from the Exploring Satellites Around Galactic Analogs (SAGA; Geha et al. 2017;

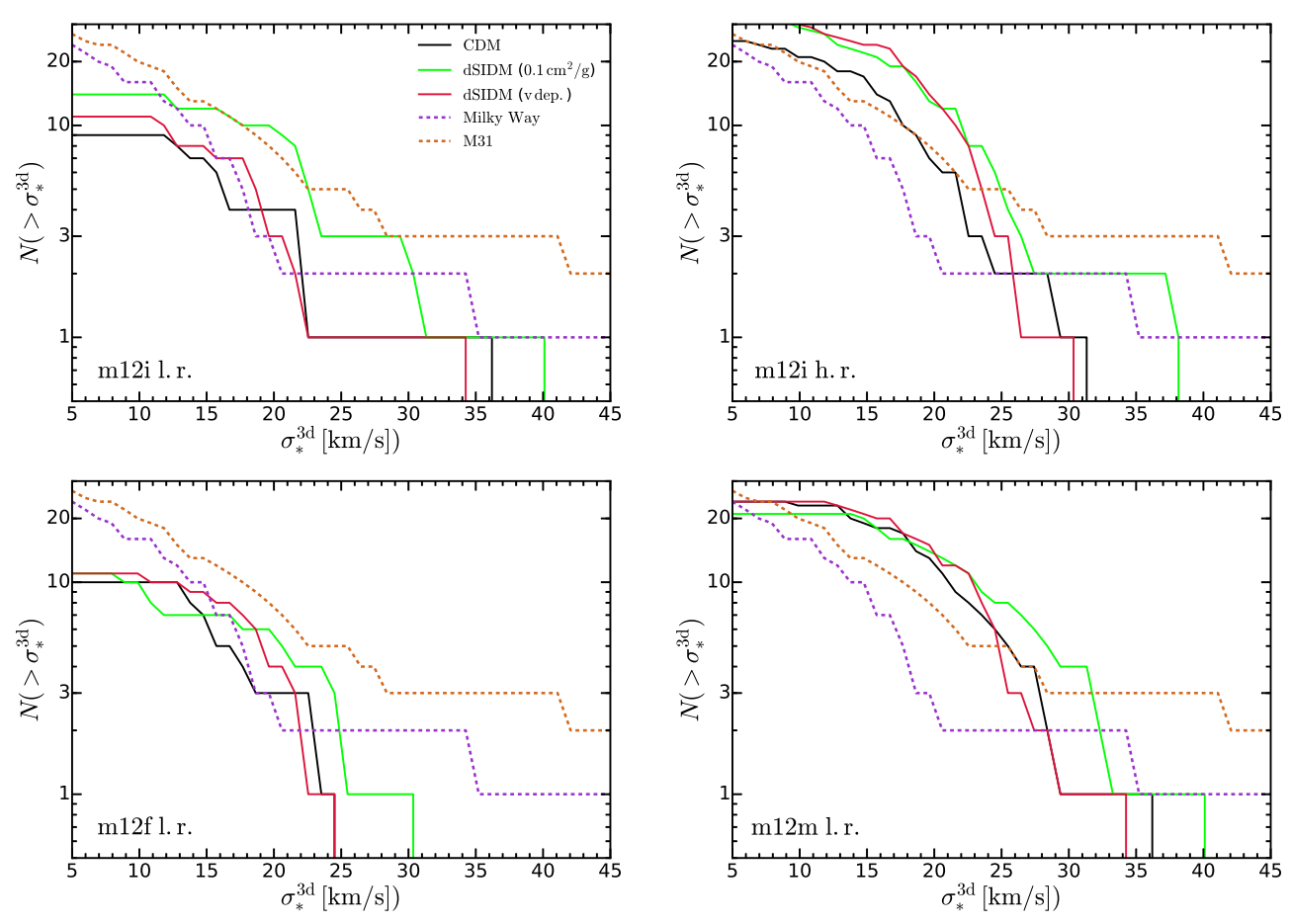


Figure 12. Cumulative count of satellites above a given stellar 3D velocity dispersion. The notation is the same as Figure 11. Similar to the stellar mass function, we find strong diversity here in both observed and simulated systems. The satellite σ_*^{3d} distributions of m12i (l.r.) and m12f are in good agreement with the Milky Way and M31 samples at $\sigma_*^{3d} \lesssim 20 \,\mathrm{km} \,\mathrm{s}^{-1}$ but do not produce enough dynamically hot satellites. On the contrary, in m12i (h.r.) and m12m, the high σ_*^{3d} end is in better agreement with the observed sample, but they tend to overpredict the number of satellites with $\sigma_*^{3d} \lesssim 25 \,\mathrm{km} \,\mathrm{s}^{-1}$. In terms of the dark matter physics tested, the dSIDM models (especially the dSIDM-c0.1 model) predict systematically higher velocity dispersions of satellites.

Mao et al. 2021) Survey Stage II.¹⁴ Each panel corresponds to one of the simulations of a Milky Way-mass galaxy. Following the convention in the previous section, we only select satellites with a stellar mass larger than 10 times the baryonic mass resolution of the simulations. This limit is indicated by the vertical dotted lines. For the observations, the Milky Way and M31 satellites extend to a stellar mass below $10^5 M_{\odot}$. All 36 complete systems in SAGA reach 100% spectroscopic coverage within the primary targeting region for galaxies with r-band absolute magnitude $M_{\rm r}$ brighter than -15.5. For galaxies fainter than $M_r = -15.5$, the survey maintains a $\sim 90\%$ spectroscopic coverage down to $M_r = -12.3$, with the completeness slightly decreasing toward fainter magnitudes. Using the color-dependent stellar mass estimates in Mao et al. (2021; modified based on Bell et al. 2003), the limit $M_{\rm r}=-12.3$ can be translated to the stellar mass of $M_*\sim 10^{6.4-7}$ assuming the typical color $0.2\lesssim (g-r)_0\lesssim 0.7$ of the confirmed satellites. This forms an estimate of the completeness limit of the SAGA surveys.

The cumulative satellite stellar mass function of simulated galaxies shows significant diversity, with m12m and m12i (h.r.) hosting \sim 10 satellites with $M_* \gtrsim 10^{6.5} M_{\odot}$ while m12f hosts

only one such satellite. This level of diversity is consistent with the scatter in mass functions revealed by the SAGA surveys. Except for m12f, which shows an apparent deficiency of massive satellites, the cumulative satellite stellar mass functions of simulated galaxies are generally consistent with observations. There are slight differences between different dark matter models. The dSIDM models with either constant or velocity-dependent cross sections do produce slightly more satellites at a given mass than CDM (i.e., slightly more massive satellites by stellar mass, for a given halo mass, on average). In the case of m12i, the total amount of resolved satellites increases by about 50% in dSIDM-c0.1 compared to CDM. In m12f and m12m, although the total number of resolved satellites does not differ significantly, massive satellites are still systematically more abundant in dSIDM models. This is likely due to suppressed tidal stripping for satellites with dark cusps built prior to infall. However, the difference is subdominant compared to the scatter found in observations, and none of the models tested is in tension with observations here.

In Figure 12, we show the cumulative number counts of satellites above a given stellar 3D velocity dispersion, σ_*^{3d} . For the satellites in simulations, σ_*^{3d} is measured at $r_{1/2}$, where it is expected to reflect the total dynamical mass (Walker et al. 2009). For the observed sample, we convert the observed line-of-sight velocity dispersion to 3D via $\sigma_*^{3d} = \sqrt{3} \ \sigma_*^{3d}$ (e.g.,

¹⁴ We acknowledge potential inconsistency in the selection criteria used between satellites in simulations and the SAGA satellites, which are selected within a line-of-sight aperture and within a line-of-sight velocity cut.

Wolf et al. 2010). The σ_*^{3d} distributions of m12i (l.r.) and m12f are consistent with the Milky Way and M31 satellites at $\sigma_*^{3d}\lesssim 20~{\rm km~s^{-1}}$ until reaching the resolution limit at low velocities. However, they do not contain as many dynamically hot satellites as the observed sample. In m12i (h.r.) and m12m, satellites exhibit systematically higher velocity dispersions (or equivalently more satellites above a given σ_*^{3d}) than m12i (l.r.) and m12f, and match better the high σ_*^{3d} end of the observed sample. But they tend to overpredict the number of satellites with $\sigma_*^{3\rm d} \lesssim 25~{\rm km~s^{-1}}$. The dSIDM models, especially the dSIDM-c0.1 model, produce more dynamically hot satellites in all four Milky Way-mass galaxies simulated. This is likely caused by larger dynamical masses of the satellites at $r_{1/2}$ on average and also a few compact outliers in dSIDM-c0.1 as shown in Figure 9. Although the comparisons here do not necessarily imply a particular model is favored or in tension with observations (given limited statistics of the host systems studied), it points to an interesting channel to study dissipative dark matter models.

In addition to the number count, the spatial distribution of satellites is also crucial in understanding the evolution of substructures in the Local Group environment. In particular, astrometric measurements have revealed that most of the Milky Way satellites orbit coherently within a spatially thin plane (e.g., Lynden-Bell 1976; Kroupa et al. 2005; Pawlowski et al. 2012) affirmed by the recent Gaia measurements (Fritz et al. 2018; Pawlowski & Kroupa 2020). The mass and spatial distributions of satellites have been studied using FIRE-2 simulations (Samuel et al. 2020, 2021) in Λ CDM. The dSIDM counterpart would be particularly interesting to explore since the dissipation promotes coherent dark rotation and triggers halo deformation as found in Paper I. This aspect along with the physical evolution of subhalos in dSIDM will be investigated in a follow-up paper of this series.

6. Summary and Conclusions

This paper is the second in a series studying galaxy formation in dissipative self-interacting dark matter. In Paper I, a suite of cosmological hydrodynamical zoom-in simulations of galaxies with dSIDM was introduced. As the starting point to study structure formation in dissipative dark matter, a simplified empirical model featuring a constant fractional energy dissipation was chosen, motivated by interactions of dark matter composites (for example, confined particles in a non-Abelian hidden sector or large stable bound states, dark *nuggets*, of asymmetric dark matter). Several interesting phenomena and physics on the dark matter side, related to dSIDM, were identified in Paper I.

In this paper, we attempt to compare predictions to basic galaxy observables affected by the underlying structural changes of dark matter halos induced by dissipative interactions. The stellar morphology, the size—mass relation, and the circular velocity profiles of both field and satellite dwarf galaxies are studied. The first tentative constraints on the dSIDM model are obtained through comparisons with observations of local dwarf galaxies.

We first study the observed morphology of the stellar component and quantitatively the size–mass relation of isolated dwarf galaxies. With moderate but not negligible interaction cross sections $((\sigma/m) \sim 1 \text{ cm}^2 \text{ g}^{-1})$, dSIDM makes the stellar content more concentrated and promotes the formation of thin stellar disks as well as neutral gas disks in massive bright

dwarfs. The simulated galaxies in these models are still consistent with observations in the plane of the galaxy size—mass relation. However, perhaps surprisingly, when the cross section becomes large enough ($\sigma/m \sim 10~{\rm cm}^2~{\rm g}^{-1}$), the stellar content of simulated dwarfs becomes even fluffier than the CDM case, owing to rotation and other emergent properties of the dark matter cusp. The dwarfs in this model lie systematically at the most diffuse observed end of the size—mass relation and thus in tension with observations.

In terms of the circular velocity profiles of simulated dwarfs, we separately consider the isolated classical and bright dwarfs in the suite as well as the satellites in the simulations of Milky Way-mass galaxies. The isolated classical dwarfs are compared to the field dwarf galaxies in the Local Group, and we find all of the dSIDM models studied survive this comparison. The isolated bright dwarfs are compared to the LSBs with HIbased circular velocity measurements. We find that the dSIDM models with $(\sigma/m) \gtrsim 0.1 \text{ cm}^2 \text{ g}^{-1}$ are in tension with observations, and the velocity-dependent model is favored. The satellites in simulated Milky Way-mass galaxies are compared to the Local Group satellites. Although we find little differences in the median and scatter of the circular velocity profiles between dark matter models, dSIDM models with $(\sigma/m) = 0.1 \text{ cm}^2 \text{ g}^{-1}$ produce outliers that agree better with the compact elliptical satellites in observations, whose analogs are missing in CDM. Although the circular velocity profiles of satellites in simulations are consistent with the observationally inferred velocity dispersions of these systems, the sizes of the simulated satellites are systematically larger. However, this is potentially subject to selection bias in observations and could also be a resolution effect. Further h.r. simulations are required to resolve the central kinematic structure of satellites to give more robust predictions. Meanwhile, the stellar mass function and velocity dispersion function of satellites are studied. In dSIDM models, the number count of satellite galaxies is slightly enhanced, and the satellites are dynamically hotter, but the difference is too small to infer valid constraints on the models.

In conclusion, it is at the mass scale of isolated bright dwarfs that the dSIDM models with constant cross sections face tentative constraints. The models with $(\sigma/m) \gtrsim 0.1 \text{ cm}^2 \text{ g}^{-1}$ are in tension with H I-based circular velocity measurements. The constraints are much weaker in lower-mass isolated dwarfs or satellites of Milky Way–mass hosts. Since as shown in Paper I the dSIDM-related phenomena strictly depend on the dissipation timescale, which is inversely proportional to the product of $f_{\rm diss}$ and (σ/m) , the tentative constraints derived here can be translated to other $f_{\rm diss}$ values giving the combined constraints, $f_{\rm diss}$ (σ/m) $\lesssim 0.075 \, {\rm cm}^2 \, {\rm g}^{-1}$. The constraints here should be treated with caution since we are limited by the number of simulated isolated halos at each representative mass scale. In addition, the systematical uncertainties in interpreting the rotation curve measurements in observations (e.g., Downing & Oman 2023) and the potential bias of H I-selected galaxies are still open questions in the field. In future work, it would be helpful to improve the robustness of the tentative constraints here with better statistics of simulations (simulating a greater variety and unbiased sample of dwarf galaxies). Meanwhile, the improved resolution would help to resolve the central structure of satellite galaxies, and in particular to investigate the implication of dSIDM in explaining the diversity of dwarf compactness in the Local Group.

Acknowledgments

Support for X.S. and P.F.H. was provided by the National Science Foundation (NSF) Research grants 1911233, 20009234, 2108318, the NSF Faculty Early Career Development Program (CAREER) grant 1455342, the National Aeronautics and Space Administration (NASA) grants 80NSSC18K0562, HST-AR-15800. Numerical calculations were run on the supercomputer Frontera at the Texas Advanced Computing Center (TACC) under the allocations AST21010 and AST20016 supported by the NSF and TACC, and NASA HEC SMD-16-7592. F.J. is supported by the Troesh scholarship. M.B.K. acknowledges support from NSF CAREER award AST-1752913, NSF grants AST-1910346 and AST-2108962, NASA grant NNX17AG29G, and HST-AR-15006, HST-AR-15809, HST-GO-15658, HST-GO-15901, HST-GO-15902, HST-AR-16159, and HST-GO-16226 from the Space Telescope Science Institute (STScI), which is operated by AURA, Inc., under NASA contract NAS5-26555. A.W. received support from NSF grants CAREER 2045928 and 2107772; NASA Astrophysics Theory Program (ATP) grant 80NSSC20K0513; HST grants AR-15809, GO-15902, GO-16273 from STScI. This research made use of data from the SAGA Survey (https://sagasurvey.org). The SAGA Survey was supported by NSF collaborative grants AST-1517148 and AST-1517422 and by HeisingSimons Foundation grant 2019-1402.

Data Availability

The simulation data of this work was generated and stored on the supercomputing system Frontera at the Texas Advanced Computing Center (TACC), under the allocations AST20010/AST20016 supported by the NSF and TACC, and NASA HEC SMD-16-7592. The CDM FIRE-2 simulations are publicly available (Wetzel et al. 2023) at http://flathub.flatironinstitute.org/fire. However, the data of the dSIDM simulations used in this article cannot be shared publicly immediately, since the series of paper is still in development. The data will be shared on reasonable request to the corresponding author.

Appendix A Resolution Dependence of Satellite Properties

The analysis above utilizes both l.r. and h.r. Milky Waymass galaxies in the simulation suite. However, the satellite structure could be resolution dependent. This can arise from two primary causes: (1) the *N*-body relaxation of collisionless particles; and (2) the artificial burstiness of the SFH due to limited mass resolution (discreteness effects). Both can puff up the dark matter and the stellar content of low-mass galaxies artificially. For example, in Fitts et al. (2019), the test on the isolated classical dwarf m10b has shown that the $r_{1/2}$ shrinks by about a factor of 2 (despite minimal changes of the overall halo properties) when increasing the mass resolution from $m_b = 4000 M_{\odot}$, to $m_b = 62.5 M_{\odot}$. Similar resolution effects manifested in the comparison of the observed ultrafaint dwarfs with h.r. dwarf simulations in Wheeler et al. (2019).

In Figure 13, we compare the satellite circular velocity profiles from the h.r. and l.r. simulations of m12i (listed in Table 1). Aside from the median and scatter of circular velocity profiles, we also show the $(V_{1/2}, r_{1/2})$ of these satellites. The median circular velocity profile is converged, and the 1.5 σ (7% to 93% inclusion) contour moves up slightly. This indicates

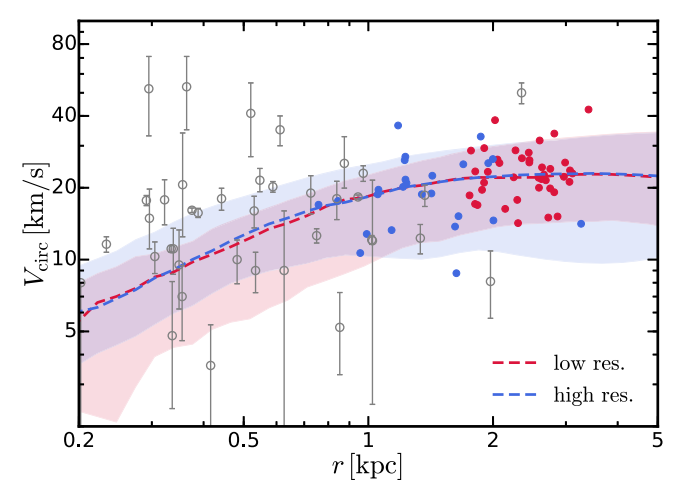


Figure 13. We compare satellite circular velocity profiles from the high- and low-resolution simulations of m12i. They are compared to the observed Milky Way/M31 satellites shown in Figure 9. Although the median circular velocity profile and the scatter do not differ appreciably between high- and low-resolution simulations, the $r_{1/2}$ values of satellites in simulations are systematically smaller in the high-resolution simulation. Compared to the observed dwarfs, even the high-resolution simulation produces fluffier stellar content for these satellites.

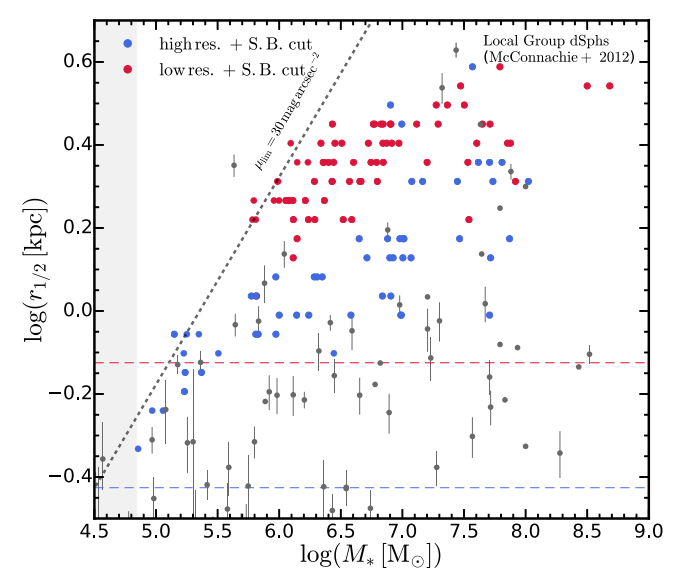


Figure 14. We compare the high- and low-resolution simulations on the plane of the size-mass relation. They are all corrected for the surface-brightness limit at $\mu_{\rm V}=30$ mag arcsec⁻². The horizontal lines indicate the radius enclosing 200 dark matter particles assuming the typical satellite central density $\rho_{\rm dm}=10^{7.5}M_{\odot}~{\rm kpc}^{-3}$. Satellites in low-resolution simulations are systematically more diffuse than their high-resolution counterparts. The resolution dependence could explain the discrepancy between the simulations with observations in this plane.

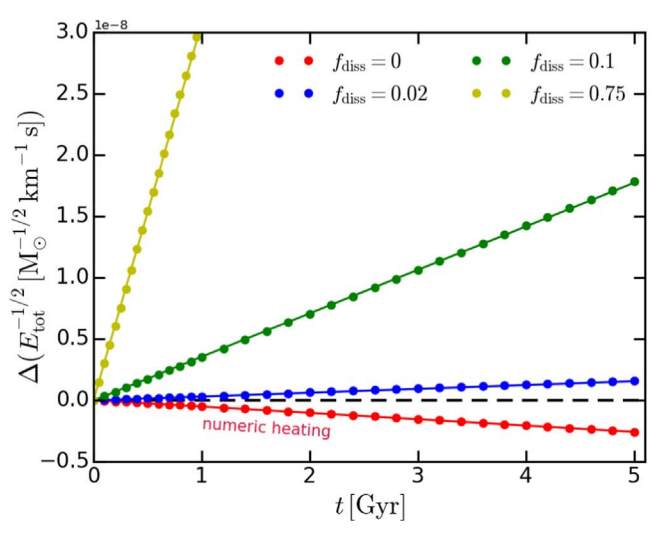
that the underlying dark matter structure of these satellites is converged at the resolution level. However, the $r_{1/2}$ values are systematically smaller in the h.r. run, and the factor by which they change is consistent with the enhancement in spatial resolution (2 times higher spatial resolution and 8 times better mass resolution). Even in the h.r. run (the mass resolution of which is still at least an order of magnitude poorer than that of isolated dwarf galaxy simulations), the stellar content of satellites can only be resolved to about 1 kpc scale, and so

the simulated small satellites are more extended than the observed satellites.

In Figure 14, we show the size–mass relations of satellites from the h.r. and l.r. simulations. The satellite stellar mass and size have been corrected for the surface-brightness cutoff at $\mu_{\rm V}=30~{\rm mag~arcsec^{-2}}$. The satellite sizes in the l.r. runs are systematically higher than the h.r. ones. The horizontal lines indicate the radius enclosing 200 dark matter particles assuming the typical satellite central density $\rho_{\rm dm} =$ $10^{7.5} M_{\odot} \text{ kpc}^{-3}$. The number 200 is suggested in Hopkins et al. (2018) as the convergence criterion in dark matter properties for FIRE-2 simulations. This limit roughly gives the minimum $r_{1/2}$ that the simulation can resolve. Certainly, we cannot conclude that the satellite sizes are fully resolved even in the h.r. runs, and it is likely that increasing the resolution will give better agreement with the observed satellites. This is supported by the fact that the simulated isolated dwarfs in the mass range $10^5-10^6 M_{\odot}$ (with baryonic mass resolution $\sim 250-500 M_{\odot}$) agree well with the observations on the sizemass plane as shown in Figures 6 and 10. The impact of resolution on satellite properties of Milky Way-mass hosts will be explored more in the upcoming Triple Latte simulations (with baryonic mass resolution $\sim 880M_{\odot}$; Wetzel et al. in prep).

Appendix B Numeric Implementation of Dark Matter Self-interactions

Dark matter self-interactions are simulated in a Monte-Carlo fashion following the implementation in Rocha et al. (2013). At each time step, for each pair of SIDM particles, the self-interaction rate (and therefore the scattering probability in the time step) is evaluated based on the *overlapped* mass and relative velocity of the two particles smoothed by a cubic spline kernel. The smoothing lengths of SIDM particles are determined by the local SIDM density estimated from kernel-smoothed neighbor particles (i.e., \tilde{n}_{SIDM} $h_{\text{i}}^3 = N_{\text{ngb}}$; an iterative approach is required to solve smoothing lengths for all SIDM particles). This is the same algorithm used for the adaptive gravitational softening (Hopkins 2015). The default neighbor number is $N_{\text{ngb}} = 32$.



After the scattering probabilities are determined, the scatterings of SIDM particles are realized in a Monte-Carlo fashion. In the center-of-momentum frame, the postscattering velocities of SIDM particles are isotropic and are reduced by a constant factor according to the $f_{\rm diss}$ parameter defined. The momentum conservation is explicitly guaranteed. However, if there are multiple scatterings of a single particle in the same time step, all velocity kicks are simply summed up at the end of the time step, rather than executed in a well-defined order. Thus, the energy is not necessarily conserved in such cases. To avoid multiple scatterings of a SIDM particle in the same step, we adopt the criterion proposed in Rocha et al. (2013). For a given SIDM particle, the time step is adjusted so that the maximum probability of interaction for any pair involving this particle is smaller than 0.2.

B.1. Numeric Heating and Its Potential Impact

As mentioned above, the pair-wise interactions that get sampled at each time step are not executed in a well-defined order. If there are multiple scattering events on the same particle, the momentum is explicitly conserved, but the energy is not, leading to artificial heating.

We can estimate this effect in the following. Since the maximum interaction probability for each particle is capped at 0.2, the tail of the probability density function that $N_{\text{scatter}} > 1$ is $P_{\text{tail}} \simeq 0.02$ assuming a Poisson distribution of N_{scatter} with a mean value 0.2. For a system consisting of N SIDM particles of equal mass, the artificial heating rate can be estimated as

$$\mathcal{H} = \frac{1}{2} N P_{\text{tail}} \frac{\beta E_{\text{single}}^{\text{kin}}}{t_{\text{coll}}} = \frac{1}{2} P_{\text{tail}} \frac{\beta E_{\text{tot}}^{\text{kin}}}{t_{\text{coll}}}$$
(B1)

where the fudge factor 1/2 accounts for double counting, β is an order-unity constant, $E_{\rm single}^{\rm kin}$ is the (average) kinetic energy of a single particle, and $E_{\rm tot}^{\rm kin}$ is the total kinetic energy of all particles. The $t_{\rm coll}$ is the collision timescale of dark matter

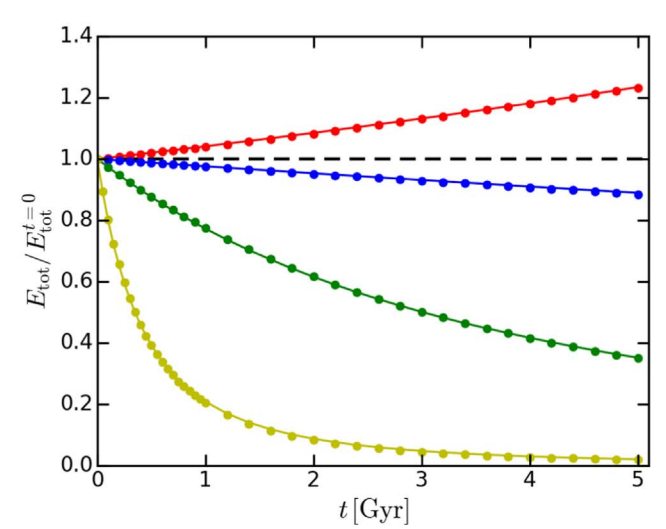


Figure 15. The right panel shows the time evolution of the total kinetic energy of the system normalized by the initial value. The left panel shows the same energy evolution but in terms of the change in $E_{\text{tot}}^{-1/2}$, which can be compared directly with the linear relationship predicted from analytical calculations. In the analytical solution (assuming an MB velocity distribution), the change in $E_{\text{tot}}^{-1/2}$ linearly depends on time, which is shown with the solid lines. Simulation results are shown with solid points. We show the results of simulations assuming $f_{\text{diss}} = 0$, 0.02, 0.1, 0.75. The simulation results agree perfectly with the analytical solutions. The black horizontal dashed line indicates the case where E_{tot} is conserved. The increase of energy in the $f_{\text{diss}} = 0$ case is caused by numeric heating.

(Equation (3) in Paper I)

$$t_{\rm coll} \simeq 103 \text{ Myr} \left(\frac{\rho}{10^9 M_{\odot} / \text{ kpc}^3} \right)^{-1} \left(\frac{(\sigma/m)}{1 \text{ cm}^2 \text{ g}^{-1}} \right)^{-1} \left(\frac{\sigma_{\rm 1d}}{20 \text{ km s}^{-1}} \right)^{-1},$$
(B2)

where σ_{1d} is the 1D velocity dispersion.

This artificial heating term is about $1/P_{\rm tail} = 50$ times weaker than the thermal conduction rate. In addition, for applications in cosmological simulations, the acceleration criterion of time stepping (Hopkins et al. 2018) will regulate the time step of the order of the local freefall time

$$t_{\rm ff} \equiv \sqrt{\frac{3\pi}{32 \ G \ \rho}} \simeq 8 \ {\rm Myr} \left(\frac{\rho}{10^9 M_{\odot}/\ {\rm kpc}^3}\right)^{-1/2},$$
 (B3)

where we have plugged in the typical central densities of simulated dwarf galaxies. For our simulated cross-sectional values, $t_{\rm ff} \lesssim t_{\rm coll}$ is guaranteed. Therefore, the mean value of $N_{\rm scatter}$ per time step will drop well below 0.2, and the artificial heating term per time step will be further suppressed quadratically, $\propto P_{\rm tail} \propto (\bar{N}_{\rm scatter}/0.2)^2 \propto (t_{\rm dyn}/t_{\rm coll})^2$. This numerical heating term will not cast any significant impact on the simulations used in the main text of this paper.

B.2. Cooling from Dissipative Dark Matter Self-interactions

The cooling rate from SIDM dissipation is by definition

$$C \equiv \frac{1}{2} N \frac{E_{\text{single}}^{\text{kin}}}{t_{\text{diss}}} = \frac{1}{2} \frac{E_{\text{tot}}^{\text{kin}}}{t_{\text{diss}}}$$
(B4)

where $t_{\rm diss}$ is the dissipation time given in Paper I (from a thermal expectation of the cooling term), and the fudge factor 1/2 again accounts for double counting.

B.3. Numeric Tests and Convergence

For the *N*-body simulations of *cold* collisionless particles with self-gravity, a numeric convergence against a particle number/spatial resolution/softening scheme/gravity solver has been studied extensively. For additional elastic dark matter self-interactions, Rocha et al. (2013) proved the convergence of the numerical collision operator to the physical one in the Boltzmann equation. In their idealized tests, the scattering rate converges to the theoretical value when the smoothing kernel is comparable to or larger than the separation of background particles. This is guaranteed in our adaptive choice of kernel sizes.

Specifically for dissipative dark matter self-interactions, we perform a series of numeric tests where particles are uniformly spawned with an isotropic velocity distribution and no self-gravity. The self-interaction cross section is set to a constant, $(\sigma/m) = 1 \text{ cm}^2 \text{ g}^{-1}$. The dissipation factor is varied in $f_{\text{diss}} = 0$, 0.02, 0.1, 0.75. We initialize $N = 10^6$ dark matter particles, with mass $m = 10^5 M_{\odot}$, in a periodic box of sidelength 10 kpc. The mass density of the box mimics the typical central density of a dwarf galaxy. The initial velocity field follows the Maxwell–Boltzmann (MB) distribution with 1D velocity dispersion, $\sigma_{\rm v} = 100 \, {\rm km \, s}^{-1}$. The evolution of the total kinetic energy is characterized by

$$\frac{dE_{\text{tot}}^{\text{kin}}}{dt} = \mathcal{H} - \mathcal{C}.$$
 (B5)

If we assume the box is uniform and the velocity distribution is well approximated by the MB distribution at any time of the test run, we have $\mathrm{d}E_{\mathrm{tot}}^{\mathrm{kin}}=3\,N\,m\,\sigma_{\mathrm{v}}^2/2$, where σ_{v} is the 1D velocity dispersion of the system. Meanwhile, both the heating and the cooling times are uniquely determined by σ_{v} (thus, $E_{\mathrm{tot}}^{\mathrm{kin}}$; see the calculation of t_{coll} and t_{diss} in Paper I). The above equation can be integrated analytically.

In Figure 15, we show the evolution of the total kinetic energy of the system, where the simulation results are shown in solid points, and the analytical solutions are shown in lines. Using the $f_{\text{diss}} = 0$ run (eSIDM), we calibrate the constant β in the heating term to be ~ 0.94 . For the other three dissipative cases, the simulation results agree perfectly with the analytical solutions. The cooling process is quasistatic (the velocity distribution maintains MB-like) since self-interactions keep the system in thermal equilibrium. The cooling behavior of the system is independent of the scale of the velocity field, as expected from the analytical solutions. Furthermore, we also perform simulations with $N_{\rm ngb} = 64$ or better mass resolution or different initial velocity distributions. None of these has an impact on the results. The tests here demonstrate the accuracy of the numerical implementation in modeling dissipative interactions of dark matter.

Besides these idealized simulations, in Paper I, we have tested the convergence of the dwarf galaxy simulation results against the numeric resolution, softening length, and whether baryonic physics is included. That represents test problems where dissipative SIDM interactions are coupled to gravity. The density profile and velocity dispersion curve are in decent agreement with the analytical solution of a subsonic, stable cooling flow. Therefore, we conclude that, even though these numeric tests cannot guarantee the convergence to the physical solution in any circumstances, we find strong enough evidence that it does converge in reasonable astrophysical conditions.

ORCID iDs

Xuejian Shen https://orcid.org/0000-0002-6196-823X Philip F. Hopkins https://orcid.org/0000-0003-3729-1684 Lina Necib https://orcid.org/0000-0003-2806-1414 Fangzhou Jiang https://orcid.org/0000-0001-6115-0633 Michael Boylan-Kolchin https://orcid.org/0000-0002-9604-343X

Andrew Wetzel https://orcid.org/0000-0003-0603-8942

References

Aalbers, J., Akerib, D. S., Akerlof, C. W., et al. 2023, PhRvL, 131, 041002
Ackerman, L., Buckley, M. R., Carroll, S. M., & Kamionkowski, M. 2009, PhRvD, 79, 023519

Akerib, D. S., Araújo, H. M., Bai, X., et al. 2014, PhRvL, 112, 091303
Alves, D. S. M., Behbahani, S. R., Schuster, P., & Wacker, J. G. 2010, JHEP, 2010, 113

Anglés-Alcázar, D., Faucher-Giguère, C.-A., Kereš, D., et al. 2017a, MNRAS, 470, 4698

Anglés-Alcázar, D., Faucher-Giguère, C.-A., Quataert, E., et al. 2017b, MNRAS, 472, L109

Aprile, E., Aalbers, J., Agostini, F., et al. 2018, PhRvL, 121, 111302
Aprile, E., Alfonsi, M., Arisaka, K., et al. 2012, PhRvL, 109, 181301
Arkani-Hamed, N., Finkbeiner, D. P., Slatyer, T. R., & Weiner, N. 2009, PhRvD, 79, 015014

Banerjee, A., Adhikari, S., Dalal, N., More, S., & Kravtsov, A. 2020, JCAP, 2020, 024

Bechtol, K., Drlica-Wagner, A., Balbinot, E., et al. 2015, ApJ, 807, 50 Behroozi, P. S., Wechsler, R. H., & Wu, H.-Y. 2013, ApJ, 762, 109

```
Bell, E. F., McIntosh, D. H., Katz, N., & Weinberg, M. D. 2003, ApJS,
   149, 289
Bertone, G. 2010, Natur, 468, 389
Bertone, G., Hooper, D., & Silk, J. 2005, PhR, 405, 279
Blennow, M., Clementz, S., & Herrero-Garcia, J. 2017, JCAP, 2017, 048
Blumenthal, G. R., Faber, S. M., Primack, J. R., & Rees, M. J. 1984, Natur,
   311, 517
Boddy, K. K., Feng, J. L., Kaplinghat, M., & Tait, T. M. P. 2014, PhRvD, 89,
Boddy, K. K., Kaplinghat, M., Kwa, A., & Peter, A. H. G. 2016, PhRvD, 94,
   123017
Boylan-Kolchin, M., Bullock, J. S., & Kaplinghat, M. 2011, MNRAS,
   415, L40
Boylan-Kolchin, M., Bullock, J. S., & Kaplinghat, M. 2012, MNRAS,
   422, 1203
Brooks, A. M., & Zolotov, A. 2014, ApJ, 786, 87
Bryan, G. L., & Norman, M. L. 1998, ApJ, 495, 80
Buck, T., Macciò, A. V., Dutton, A. A., Obreja, A., & Frings, J. 2019,
      IRAS, 483, 1314
Buckley, M. R., & Peter, A. H. G. 2018, PhR, 761, 1
Bullock, J. S., & Boylan-Kolchin, M. 2017, ARA&A, 55, 343
Carlin, J. L., Sand, D. J., Price, P., et al. 2016, ApJ, 828, L5
Carlson, E. D., Machacek, M. E., & Hall, L. J. 1992, ApJ, 398, 43
Chacko, Z., Craig, N., Fox, P. J., & Harnik, R. 2017, JHEP, 2017, 23
Chacko, Z., Goh, H.-S., & Harnik, R. 2006, JHEP, 01, 108
Chan, T. K., Kereš, D., Oñorbe, J., et al. 2015, MNRAS, 454, 2981
Cline, J. M., Liu, Z., Moore, G. D., & Xue, W. 2014, PhRvD, 90, 015023
Cole, S., Lacey, C. G., Baugh, C. M., & Frenk, C. S. 2000, MNRAS, 319, 168
Colpi, M., Mayer, L., & Governato, F. 1999, ApJ, 525, 720
Creasey, P., Sameie, O., Sales, L. V., et al. 2017, MNRAS, 468, 2283
Crnojević, D., Sand, D. J., Spekkens, K., et al. 2016, ApJ, 823, 19
Cyr-Racine, F.-Y., Ge, F., & Knox, L. 2022, PhRvL, 128, 201301
Cyr-Racine, F.-Y., & Sigurdson, K. 2013, PhRvD, 87, 103515
Dalcanton, J. J., & Hogan, C. J. 2001, ApJ, 561, 35
Dark Energy Survey Collaboration, Abbott, T., Abdalla, F. B., et al. 2016,
   MNRAS, 460, 1270
Das, A., & Dasgupta, B. 2018, PhRvD, 97, 023002
Davis, M., Efstathiou, G., Frenk, C. S., & White, S. D. M. 1985, ApJ, 292, 371
de Blok, W. J. G., McGaugh, S. S., & Rubin, V. C. 2001, AJ, 122, 2396
de Laix, A. A., Scherrer, R. J., & Schaefer, R. K. 1995, ApJ, 452, 495
Despali, G., Sparre, M., Vegetti, S., et al. 2019, MNRAS, 484, 4563
Detmold, W., McCullough, M., & Pochinsky, A. 2014, PhRvD, 90, 115013
Di Cintio, A., Brook, C. B., Macciò, A. V., et al. 2014, MNRAS, 437, 415
Diemand, J., Zemp, M., Moore, B., Stadel, J., & Carollo, C. M. 2005,
   MNRAS, 364, 665
Dooley, G. A., Peter, A. H. G., Vogelsberger, M., Zavala, J., & Frebel, A.
   2016, MNRAS, 461, 710
Downing, E. R., & Oman, K. A. 2023, MNRAS, 522, 3318
Drlica-Wagner, A., Bechtol, K., Mau, S., et al. 2020, ApJ, 893, 47
Drlica-Wagner, A., Bechtol, K., Rykoff, E. S., et al. 2015, ApJ, 813, 109
Dutton, A. A., Macciò, A. V., Frings, J., et al. 2016, MNRAS, 457, L74
Eigenthaler, P., Puzia, T. H., Taylor, M. A., et al. 2018, ApJ, 855, 142
El-Badry, K., Quataert, E., Wetzel, A., et al. 2018, MNRAS, 473, 1930
Elbert, O. D., Bullock, J. S., Garrison-Kimmel, S., et al. 2015, MNRAS,
Enzi, W., Murgia, R., Newton, O., et al. 2021, MNRAS, 506, 5848
Essig, R., McDermott, S. D., Yu, H.-B., & Zhong, Y.-M. 2019, PhRvL, 123,
   121102
Fan, J., Katz, A., Randall, L., & Reece, M. 2013, PDU, 2, 139
Fattahi, A., Navarro, J. F., Sawala, T., et al. 2016, MNRAS, 457, 844
Faucher-Giguère, C.-A., Lidz, A., Zaldarriaga, M., & Hernquist, L. 2009, ApJ,
Feldmann, R., Quataert, E., Faucher-Giguère, C.-A., et al. 2023, MNRAS,
   522, 3831
Feng, J. L., Kaplinghat, M., Tu, H., & Yu, H.-B. 2009, J. Cosmol. Astropart.
   Phys., 2009, 004
Feng, J. L., Kaplinghat, M., & Yu, H.-B. 2010, PhRvL, 104, 151301
Finkbeiner, D. P., & Weiner, N. 2016, PhRvD, 94, 083002
Firmani, C., D'Onghia, E., Avila-Reese, V., Chincarini, G., & Hernández, X.
  2000, MNRAS, 315, L29
Fischer, M. S., Brüggen, M., Schmidt-Hoberg, K., et al. 2022, MNRAS,
Fitts, A., Boylan-Kolchin, M., Bozek, B., et al. 2019, MNRAS, 490, 962
Fitts, A., Boylan-Kolchin, M., Elbert, O. D., et al. 2017, MNRAS, 471, 3547
Flaugher, B., Diehl, H. T., Honscheid, K., et al. 2015, AJ, 150, 150
Flores, R. A., & Primack, J. R. 1994, ApJ, 427, L1
```

```
Foot, R. 2004, IJMPD, 13, 2161
Foot, R. 2013, PhRvD, 88, 023520
Foot, R., & Vagnozzi, S. 2015a, PhRvD, 91, 023512
Foot, R., & Vagnozzi, S. 2015b, PhLB, 748, 61
Fraternali, F., Tolstoy, E., Irwin, M. J., & Cole, A. A. 2009, A&A, 499, 121
Frenk, C. S., & White, S. D. M. 2012, AnP, 524, 507
Fritz, T. K., Battaglia, G., Pawlowski, M. S., et al. 2018, A&A, 619, A103
Fry, A. B., Governato, F., Pontzen, A., et al. 2015, MNRAS, 452, 1468
Gan, J., Kang, X., van den Bosch, F. C., & Hou, J. 2010, MNRAS, 408, 2201
Garrison-Kimmel, S., Boylan-Kolchin, M., Bullock, J. S., & Kirby, E. N. 2014,
         AS, 444, 222
Garrison-Kimmel, S., Hopkins, P. F., Wetzel, A., et al. 2019a, MNRAS,
   487, 1380
Garrison-Kimmel, S., Wetzel, A., Hopkins, P. F., et al. 2019b, MNRAS,
Geha, M., Wechsler, R. H., Mao, Y.-Y., et al. 2017, ApJ, 847, 4
Gemmell, C., Roy, S., Shen, X., et al. 2023, arXiv:2311.02148
Gentile, G., Salucci, P., Klein, U., Vergani, D., & Kalberla, P. 2004, MNRAS,
   351, 903
Genzel, R., Price, S. H., Übler, H., et al. 2020, ApJ, 902, 98
Governato, F., Brook, C., Mayer, L., et al. 2010, Natur, 463, 203
Governato, F., Zolotov, A., Pontzen, A., et al. 2012, MNRAS, 422, 1231
Gregory, A. L., Collins, M. L. M., Read, J. I., et al. 2019, MNRAS, 485, 2010
Gresham, M. I., Lou, H. K., & Zurek, K. M. 2018, PhRvD, 98, 096001
Grudić, M. Y., Boylan-Kolchin, M., Faucher-Giguère, C.-A., & Hopkins, P. F.
   2020, MNRAS, 496, L127
Hafen, Z., Faucher-Giguère, C.-A., Anglés-Alcázar, D., et al. 2019, MNRAS,
   488, 1248
Hogan, C. J., & Dalcanton, J. J. 2000, PhRvD, 62, 063511
Hopkins, P. F. 2015, MNRAS, 450, 53
Hopkins, P. F., Chan, T. K., Garrison-Kimmel, S., et al. 2020, MNRAS,
   492, 3465
Hopkins, P. F., Gurvich, A. B., Shen, X., et al. 2023a, MNRAS, 525, 2241
Hopkins, P. F., Hernquist, L., Martini, P., et al. 2005, ApJ, 625, L71
Hopkins, P. F., Kereš, D., Oñorbe, J., et al. 2014, MNRAS, 445, 581
Hopkins, P. F., Narayanan, D., & Murray, N. 2013, MNRAS, 432, 2647
Hopkins, P. F., Quataert, E., & Murray, N. 2012, MNRAS, 421, 3488
Hopkins, P. F., Squire, J., Chan, T. K., et al. 2021, MNRAS, 501, 4184
Hopkins, P. F., Wetzel, A., Kereš, D., et al. 2018, MNRAS, 480, 800
Hopkins, P. F., Wetzel, A., Wheeler, C., et al. 2023b, MNRAS, 519, 3154
Hryczuk, A., & Jodłowski, K. 2020, PhRvD, 102, 043024
Huo, R., Yu, H.-B., & Zhong, Y.-M. 2020, JCAP, 2020, 051
Jiang, F., Dekel, A., Freundlich, J., et al. 2019, MNRAS, 487, 5272
Jiang, F., & van den Bosch, F. C. 2016, MNRAS, 458, 2848
Kahlhoefer, F., Kaplinghat, M., Slatyer, T. R., & Wu, C.-L. 2019, JCAP,
   2019, 010
Kamada, A., Kaplinghat, M., Pace, A. B., & Yu, H.-B. 2017, PhRvL, 119,
   111102
Kaplan, D. E., Krnjaic, G. Z., Rehermann, K. R., & Wells, C. M. 2010, JCAP,
   2010, 021
Kaplinghat, M., Ren, T., & Yu, H.-B. 2020, JCAP, 2020, 027
Kaplinghat, M., Tulin, S., & Yu, H.-B. 2016, PhRvL, 116, 041302
Kaplinghat, M., Valli, M., & Yu, H.-B. 2019, MNRAS, 490, 231
Kauffmann, G., White, S. D. M., & Guiderdoni, B. 1993, MNRAS, 264, 201
Kirby, E. N., Bullock, J. S., Boylan-Kolchin, M., Kaplinghat, M., &
   Cohen, J. G. 2014, MNRAS, 439, 1015
Klypin, A., Kravtsov, A. V., Bullock, J. S., & Primack, J. R. 2001, ApJ,
   554, 903
Klypin, A., Kravtsov, A. V., Valenzuela, O., & Prada, F. 1999, ApJ, 522, 82
Koda, J., Yagi, M., Yamanoi, H., & Komiyama, Y. 2015, ApJ, 807, L2
Koposov, S. E., Belokurov, V., Torrealba, G., & Evans, N. W. 2015, ApJ,
Krnjaic, G., & Sigurdson, K. 2015, PhLB, 751, 464
Kroupa, P., Theis, C., & Boily, C. M. 2005, A&A, 431, 517
Kuzio de Naray, R., & Kaufmann, T. 2011, MNRAS, 414, 3617
Kuzio de Naray, R., McGaugh, S. S., de Blok, W. J. G., & Bosma, A. 2006,
Kuzio de Naray, R., & Spekkens, K. 2011, ApJ, 741, L29
Laevens, B. P. M., Martin, N. F., Bernard, E. J., et al. 2015b, ApJ, 813, 44
Laevens, B. P. M., Martin, N. F., Ibata, R. A., et al. 2015a, ApJ, 802, L18
Lange, R., Driver, S. P., Robotham, A. S. G., et al. 2015, MNRAS, 447, 2603
Lazar, A., Bullock, J. S., Boylan-Kolchin, M., et al. 2020, MNRAS, 497, 2393
Leitherer, C., Schaerer, D., Goldader, J. D., et al. 1999, ApJS, 123, 3
Lelli, F., McGaugh, S. S., Schombert, J. M., & Pawlowski, M. S. 2016b, ApJ,
   827, L19
Lelli, F., McGaugh, S. S., & Schombert, J. M. 2016a, AJ, 152, 157
```

```
Li, P., Lelli, F., McGaugh, S., & Schombert, J. 2020, ApJS, 247, 31
Loeb, A., & Weiner, N. 2011, PhRvL, 106, 171302
Lovell, M. R., & Zavala, J. 2023, MNRAS, 520, 1567
LSST Science Collaboration, Abell, P. A., Allison, J., et al. 2009,
  arXiv:0912.0201
Lynden-Bell, D. 1976, MNRAS, 174, 695
Ma, X., Hopkins, P. F., Boylan-Kolchin, M., et al. 2018, MNRAS, 477, 219
Ma, X., Hopkins, P. F., Faucher-Giguère, C.-A., et al. 2016, MNRAS,
   456, 2140
Madau, P., Shen, S., & Governato, F. 2014, ApJ, 789, L17
Mao, Y.-Y., Geha, M., Wechsler, R. H., et al. 2021, ApJ, 907, 85
Markevitch, M., Gonzalez, A. H., Clowe, D., et al. 2004, ApJ, 606, 819
McConnachie, A. W. 2012, AJ, 144, 4
Mihos, J. C., Durrell, P. R., Ferrarese, L., et al. 2015, ApJ, 809, L21
Miyazaki, S., Komiyama, Y., Kawanomoto, S., et al. 2018, PASJ, 70, S1
Miyazaki, S., Komiyama, Y., Sekiguchi, M., et al. 2002, PASJ, 54, 833
Mohapatra, R. N., & Teplitz, V. L. 2000, PhRvD, 62, 063506
Moore, B. 1994, Natur, 370, 629
Moore, B., Ghigna, S., Governato, F., et al. 1999, ApJ, 524, L19
Muñoz, R. P., Eigenthaler, P., Puzia, T. H., et al. 2015, ApJ, 813, L15
Muratov, A. L., Kereš, D., Faucher-Giguère, C.-A., et al. 2015, MNRAS,
   454, 2691
Nadler, E. O., Banerjee, A., Adhikari, S., Mao, Y.-Y., & Wechsler, R. H.
   2020a, ApJ, 896, 112
Nadler, E. O., Drlica-Wagner, A., Bechtol, K., et al. 2021, PhRvL, 126, 091101
Nadler, E. O., Gluscevic, V., Boddy, K. K., & Wechsler, R. H. 2019, ApJ,
Nadler, E. O., Wechsler, R. H., Bechtol, K., et al. 2020b, ApJ, 893, 48
Navarro, J. F., Frenk, C. S., & White, S. D. M. 1996, ApJ, 462, 563
Navarro, J. F., Frenk, C. S., & White, S. D. M. 1997, ApJ, 490, 493
Navarro, J. F., Hayashi, E., Power, C., et al. 2004, MNRAS, 349, 1039
Necib, L., Lisanti, M., Garrison-Kimmel, S., et al. 2019, ApJ, 883, 27
Obreja, A., Stinson, G. S., Dutton, A. A., et al. 2016, MNRAS, 459, 467
Oh, S.-H., Brook, C., Governato, F., et al. 2011, AJ, 142, 24
Oh, S.-H., Hunter, D. A., Brinks, E., et al. 2015, AJ, 149, 180
Oman, K. A., Navarro, J. F., Fattahi, A., et al. 2015, MNRAS, 452, 3650
Oñorbe, J., Boylan-Kolchin, M., Bullock, J. S., et al. 2015, MNRAS, 454, 2092
Ott, J., Stilp, A. M., Warren, S. R., et al. 2012, AJ, 144, 123
Papastergis, E., Giovanelli, R., Haynes, M. P., & Shankar, F. 2015, A&A,
   574, A113
Pawlowski, M. S., & Kroupa, P. 2020, MNRAS, 491, 3042
Pawlowski, M. S., Pflamm-Altenburg, J., & Kroupa, P. 2012, MNRAS,
   423, 1109
Pei, Y. C. 1992, ApJ, 395, 130
Peñarrubia, J., Benson, A. J., Walker, M. G., et al. 2010, MNRAS, 406, 1290
Pontzen, A., & Governato, F. 2012, MNRAS, 421, 3464
Power, C., Navarro, J. F., Jenkins, A., et al. 2003, MNRAS, 338, 14
Quinn, P. J., & Goodman, J. 1986, ApJ, 309, 472
Randall, L., & Scholtz, J. 2015, JCAP, 2015, 057
Randall, S. W., Markevitch, M., Clowe, D., Gonzalez, A. H., & Bradač, M.
  2008, ApJ, 679, 1173
Robertson, A., Massey, R., & Eke, V. 2017, MNRAS, 467, 4719
Robles, V. H., Bullock, J. S., Elbert, O. D., et al. 2017, MNRAS, 472, 2945
Robles, V. H., Kelley, T., Bullock, J. S., & Kaplinghat, M. 2019, MNRAS,
Rocha, M., Peter, A. H. G., Bullock, J. S., et al. 2013, MNRAS, 430, 81
Roy, S., Shen, X., Lisanti, M., et al. 2023, ApJ, 954, L40
Sales, L. V., Wetzel, A., & Fattahi, A. 2022, NatAs, 6, 897
Sameie, O., Yu, H.-B., Sales, L. V., Vogelsberger, M., & Zavala, J. 2020,
  PhRvL, 124, 141102
```

Samuel, J., Wetzel, A., Chapman, S., et al. 2021, MNRAS, 504, 1379

```
Samuel, J., Wetzel, A., Tollerud, E., et al. 2020, MNRAS, 491, 1471
Sand, D. J., Spekkens, K., Crnojević, D., et al. 2015, ApJ, 812, L13
Santos-Santos, I. M., Di Cintio, A., Brook, C. B., et al. 2018, MNRAS,
  473, 4392
Santos-Santos, I. M. E., Navarro, J. F., Robertson, A., et al. 2020, MNRAS,
  495, 58
Sawala, T., Frenk, C. S., Fattahi, A., et al. 2016, MNRAS, 457, 1931
Schutz, K., & Slatyer, T. R. 2015, JCAP, 2015, 021
Shen, X., Hopkins, P. F., Necib, L., et al. 2021, MNRAS, 506, 4421
Simon, J. D., Bolatto, A. D., Leroy, A., Blitz, L., & Gates, E. L. 2005, ApJ,
Spano, M., Marcelin, M., Amram, P., et al. 2008, MNRAS, 383, 297
Spergel, D. N., & Steinhardt, P. J. 2000, PhRvL, 84, 3760
Springel, V. 2005, MNRAS, 364, 1105
Stanimirović, S., Staveley-Smith, L., & Jones, P. A. 2004, ApJ, 604, 176
Stern, J., Faucher-Giguère, C.-A., Fielding, D., et al. 2021, ApJ, 911, 88
Strassler, M. J., & Zurek, K. M. 2007, PhLB, 651, 374
Taibi, S., Battaglia, G., Rejkuba, M., et al. 2020, A&A, 635, A152
Taylor, J. E., & Babul, A. 2001, ApJ, 559, 716
Tollerud, E. J., Boylan-Kolchin, M., & Bullock, J. S. 2014, MNRAS,
  440, 3511
Torrealba, G., Belokurov, V., Koposov, S. E., et al. 2019, MNRAS,
  488, 2743
Torrealba, G., Koposov, S. E., Belokurov, V., & Irwin, M. 2016, MNRAS,
  459, 2370
Tulin, S., & Yu, H.-B. 2018, Phys. Rep., 730, 1
Tulin, S., Yu, H.-B., & Zurek, K. M. 2013, PhRvD, 87, 115007
van den Aarssen, L. G., Bringmann, T., & Pfrommer, C. 2012, PhRvL, 109,
van der Marel, R. P., & Kallivayalil, N. 2014, ApJ, 781, 121
van der Wel, A., Franx, M., van Dokkum, P. G., et al. 2014, ApJ, 788, 28
van Dokkum, P. G., Abraham, R., Merritt, A., et al. 2015, ApJ, 798, L45
Vogelsberger, M., Zavala, J., & Loeb, A. 2012, MNRAS, 423, 3740
Vogelsberger, M., Zavala, J., Schutz, K., & Slatyer, T. R. 2019, MNRAS,
  484, 5437
Vogelsberger, M., Zavala, J., Simpson, C., & Jenkins, A. 2014, MNRAS,
  444, 3684
Walker, M. G., Mateo, M., Olszewski, E. W., et al. 2009, ApJ, 704, 1274
Walker, M. G., & Peñarrubia, J. 2011, ApJ, 742, 20
Wellons, S., Faucher-Giguère, C.-A., Hopkins, P. F., et al. 2023, MNRAS,
   520, 5394
Wetzel, A., & Garrison-Kimmel, S. 2020, HaloAnalysis: Read and analyze
  halo catalogs and merger trees, Astrophysics Source Code Library,
  ascl:2002.014
Wetzel, A., Hayward, C. C., Sanderson, R. E., et al. 2023, ApJS, 265, 44
Wetzel, A. R., Hopkins, P. F., Kim, J.-H., et al. 2016, ApJ, 827, L23
Wheeler, C., Hopkins, P. F., Pace, A. B., et al. 2019, MNRAS, 490, 4447
Wheeler, C., Oñorbe, J., Bullock, J. S., et al. 2015, MNRAS, 453, 1305
White, S. D. M., & Frenk, C. S. 1991, ApJ, 379, 52
Wise, M. B., & Zhang, Y. 2014, PhRvD, 90, 055030
Wise, M. B., & Zhang, Y. 2015, JHEP, 2015, 23
Wolf, J., Martinez, G. D., Bullock, J. S., et al. 2010, MNRAS, 406, 1220
Wright, A. C., Brooks, A. M., Weisz, D. R., & Christensen, C. R. 2019,
     NRAS, 482, 1176
York, D. G., Adelman, J., Anderson, John E. J., et al. 2000, AJ, 120,
Zavala, J., Vogelsberger, M., & Walker, M. G. 2013, MNRAS, 431, L20
Zeng, Z. C., Peter, A. H. G., Du, X., et al. 2022, MNRAS, 513, 4845
Zentner, A. R., & Bullock, J. S. 2003, ApJ, 598, 49
Zhang, Y. 2017, PDU, 15, 82
Zhu, Q., Marinacci, F., Maji, M., et al. 2016, MNRAS, 458, 1559
```